Atmos. Chem. Phys. Discuss., 11, 30273–30331, 2011
www.atmos-chem-phys-discuss.net/11/30273/2011/
doi:10.5194/acpd-11-30273-2011

Atmospheric Chemistry and Physics Discussions

Atmospheric dust modeling from meso to global scales with the online NMMB/BSC-Dust model – Part 2: Experimental campaigns in Northern Africa

K. Haustein[1], C. Pérez[2,3], J. M. Baldasano[1,4], O. Jorba[1], S. Basart[1], R. L. Miller[3], Z. Janjic[5], T. Black[5], S. Nickovic[6], M. C. Todd[7], and R. Washington[8]

[1]Barcelona Supercomputing Center, Earth Science Department, Barcelona, Spain
[2]International Research Institute for Climate and Society, The Earth Institute, Columbia University, New York, USA
[3]NASA Goddard Institute for Space Studies, New York, USA
[4]Environmental Modeling Laboratory, Technical University of Catalonia, Barcelona, Spain
[5]Environmental Modeling Center, National Centers for Environmental Prediction, Camp Springs, Maryland, USA

[6]Research Department, World Meteorological Organization, Geneva, Switzerland
[7]Department of Geography, University College London, London, UK
[8]Climate Research Group, Oxford University Centre for the Environment, University of Oxford, Oxford, UK

Received: 23 August 2011 – Accepted: 26 October 2011 – Published: 9 November 2011

Correspondence to: K. Haustein (post@karstenhaustein.de)

Abstract

The new online NMMB/BSC-Dust model is intended to provide short to medium-range weather and dust forecasts from regional to global scales. The companion paper (Pérez et al., 2011) develops the dust model parameterizations and provides daily to annual evaluations of the model for its global and regional configurations. Modeled aerosol optical depth (AOD) was evaluated against AERONET Sun photometers over Northern Africa, Middle East and Europe with correlations around 0.6–0.7 on average without dust data assimilation. In this paper we analyze in detail the behavior of the model using data from the Saharan Mineral dUst experiment (SAMUM-1) in 2006 and the Bodélé Dust Experiment (BoDEx) in 2005. AOD from satellites and Sun photometers, vertically resolved extinction coefficients from lidars and particle size distributions at the ground and in the troposphere are used, complemented by wind profile data and surface meteorological measurements.

All simulations were performed at the regional scale for the Northern African domain at the expected operational resolution of 25 km. Model results for SAMUM-1 generally show good agreement with satellite data over the most active Saharan dust sources. The model reproduces the AOD from Sun photometers close to sources and after long-range transport, and the dust size spectra at different height levels. At this resolution, the model is not able to reproduce a large haboob occurred during the campaign. Some deficiencies are found concerning the vertical distribution. The mixing height is underestimated which may be attributed to poor soil initial conditions. For the BoDEx period, particular attention is paid to understand the dust model behavior in relation with the low level jet (LLJ) in the Bodélé. The diurnal temperature cycle depends strongly on the soil moisture, which is underestimated in the NCEP analysis used for model initialization. The daily maximum surface wind speeds are underestimated up to 50 % in some days even when using a more accurate soil moisture initialization. The dust plume over the Bodélé is well reproduced by the model and the reductions in the threshold friction velocity substantially reduce the negative AOD bias in the model due

ACPD
11, 30273–30331, 2011

to wind speed underestimation. The LLJ is also well reproduced, which is remarkable given the rather poor model initialization with NCEP-FNL data.

1 Introduction

Mineral dust emitted from arid and semi-arid areas is one of the most important sources of atmospheric aerosol mass and significantly impacts the Earth's climate system. Although there has been significant progress in estimating and modeling the dust cycle in the last decades, the magnitude of the dust net direct radiative forcing still remains uncertain varying between −0.56 and +0.1 $W m^{-2}$ (IPCC, 2007). Neither the annual global dust emission nor its spatial distribution is sufficiently well quantified, with the first to be in the range from 1000 to 2150 $Mt\,year^{-1}$ (Zender et al., 2004; IPCC, 2007). Besides changing the global and regional energy balance by absorbing and scattering shortwave and longwave radiation (Houghton et al., 2001), dust transported by winds modifies atmospheric heating rates, temperatures and stability, influences the hydrological cycle (e.g. Sokolik and Toon, 1996; Tegen, 2003; Myhre et al., 2003; Miller et al., 2004; Helmert et al., 2007) and impacts human health (Yin et al., 2005), particularly close to source areas.

In the last few decades numerical models have been designed to reproduce the dust cycle allowing to estimate the influence of mineral dust on the climate system. Dust models are also required for short to medium range air quality forecast applications. To this end, several models have been developed with some of them providing daily forecast products, e.g. the Dust REgional Atmospheric Model (BSC-DREAM) (Nickovic et al., 2001), the SKIRON model (Kallos et al., 1997), CHIMERE-Dust model (Menut et al., 2005), the Navy Aerosol Analysis and Prediction System (NAAPS) (Christensen, 1997), the JMA-MASINGAR dust model (Tanaka and Chiba, 2005), or the ECMWF-IFS (Morcrette et al., 2008). The BSC-DREAM model was further developed and refined in the last years (Pérez et al., 2006b, 2007; Papayannis et al., 2007; Haustein et al., 2009; Papanastasiou et al., 2010; Seifert et al., 2010) at the Barcelona Supercomputing

ACPD
11, 30273–30331, 2011

Center (BSC).

In the companion paper (Pérez et al., 2011), we described the NMMB/BSC-Dust, a new online multi-scale atmospheric dust model, designed and developed at the BSC in collaboration with NOAA/National Centers for Environmental Prediction (NCEP), NASA Goddard Institute for Space Studies and the International Research Institute for Climate and Society (IRI). The dust model is embedded into the Non-hydrostatic Multiscale Model NMMB (Janjic et al., 2005, 2011; Janjic and Black, 2007) and will provide short to medium-range dust forecasts for both regional and global domains. In Pérez et al. (2011), we evaluated monthly and annual means of the global configuration of the model against the AeroCom dust benchmark dataset for year 2000 including surface concentration, deposition and aerosol optical depth (AOD), as well as the daily AOD variability in a regional domain at high resolution covering Northern Africa, Middle East and Europe against the AErosol RObotic NETwork (AERONET) AOD for the year 2006. The NMMB/BSC-Dust provides a good description of the horizontal distribution and temporal variability of the dust. Daily AOD correlations at the regional scale were around 0.6–0.7 on average without dust data assimilation. At the global scale the model lies within the top range of AeroCom dust models in terms of performance statistics for surface concentration, deposition and AOD.

In this contribution, we use the data from two field experiments: SAMUM-1 (Heintzenberg, 2009) and BoDEx (Washington et al., 2006a), complemented by in-situ remote-sensing data and satellite retrievals to evaluate and analyze the behavior of the model in Northern Africa. The data from both campaigns have already been used for extensive model evaluation (e.g. Tegen et al., 2006; Bouet et al., 2007; Todd et al., 2007, 2008a; Haustein et al., 2009; Heinold et al., 2009; Müller et al., 2009; Otto et al., 2009, 2011). The first phase of SAMUM-1 took place in May/June 2006 at three sites in Morocco accompanied by several overflights of two research aircraft. The observational dataset includes ground-based (Raman and backscatter) and on-board High-Spectral-Resolution Lidar (HSRL) profiles, surface and tropospheric dust size distribution, aerosol mass concentration and chemical composition, dust sample

ACPD
11, 30273–30331, 2011

microscopic and optical properties, Sun photometer data as well as basic meteorological parameters. The BoDEx experimental campaign took place in March 2005 at the Bodélé Depression (in the Djourab of Northern Chad) which contributes well to over half of the annual dust that is produced in West Africa each year (Washington et al., 2003). Here, we mainly focus on the ability of the model to represent the local meteorology, notably the low-level jet feature (LLJ), and the dust emission pattern in this prolific dust source.

The paper is organized as follows. We summarize the model features presented in Pérez et al. (2011) in Sect. 2. In Sect. 3 we introduce the observational data from the two field campaigns and those derived from ground based and satellite remote sensing. Sect. 4 includes the results and discussion and we conclude in Sect. 5.

2 Model description

2.1 The NMMB/BSC-dust model

A detailed description of the model can be found in the companion paper (Pérez et al., 2011). This section summarizes the main characteristics of the NMMB/BSC-Dust model.

The NCEP-NMMB is the evolution of the well known NCEP/Eta (Janjic, 1990, 1994) and NCEP/WRF-NMME (Janjic et al., 2001; Janjic, 2003) with updated meteorological core, built on many decades of numerical weather prediction (NWP) experience. The model (Janjic and Black, 2006; Janjic et al., 2010, 2011) provides an improved numerical environment for the physical and dynamical schemes, essential to be able to increase the model resolution, the forecast domain or the number of incorporated physical and dynamical processes. The model is unified for regional and global simulations and has the non-hydrostatic option as add-on module (Janjic and Black, 2006; Janjic et al., 2010). In contrast to the WRF-NMME, it is now developed on the Arakawa B-grid (Arakawa and Lamb, 1977) with regular latitude-longitude coordinates for the global

ACPD
11, 30273–30331, 2011

configuration and rotated latitude-longitude coordinates for the regional configuration. Lorenz vertical staggered grid with pressure-sigma hybrid coordinate is used.

Dust is transported as the other tracers in the NMMB model. Tracer advection is Eulerian, positive-definite and monotonic. The Adams-Bashforth scheme is used for horizontal advection and the Crank-Nicholson scheme for vertical advection. For the horizontal diffusion the model uses a second order scheme. Dust emission and vertical diffusion, sedimentation, dry and wet deposition, and dust radiative feedback are also represented in the model. The default radiation scheme is the Geophysical Fluid Dynamics Laboratory (GFDL) package with longwave (LW) radiation after Fels and Schwarzkopf (1975) and shortwave (SW) radiation after Lacis and Hansen (1974). In order to take into account the effects of aerosols and mineral dust interactively, the rapid radiative transfer model (RRTM) (Mlawer et al., 1997) was implemented in the NMMB/BSC-Dust.

The dust emission scheme requires the calculation of the horizontal saltation and the vertical dust flux. It includes the threshold friction velocity $u_{*\mathrm{thr}}$ which is the minimum friction velocity required to suspend soil particles in dependence of land surface conditions, surface wind speed and soil moisture (Bagnold, 1941; Iversen and White, 1982; Fécan et al., 1999). In this contribution we use the aeolian surface roughness over sand surfaces based on the roughness data set at $1/4^\circ \times 1/4^\circ$ spatial resolution provided by Laurent et al. (2008). The smooth surface roughness is calculated according to Marticorena and Bergametti (1995). For the saltation dust flux, the parameterization suggested in Marticorena and Bergametti (1995) with the horizontal flux formulation after White (1979) is used. Four parent soil size categories following Tegen et al. (2002) are taken into account (clay, silt, fine/medium sand, and coarse sand) covering a size range from < 2 to 1000 µm. Soil mass fractions are calculated from the 12 top soil texture classes of the hybrid STATSGO-FAO 1 km database.

The straight forward approach for the vertical flux after Marticorena and Bergametti (1995) is used, with and empirical horizontal to vertical flux ratio or sandblasting mass efficiency α. For sources we use the topographic preferential source approach after

ACPD
11, 30273–30331, 2011

Ginoux et al. (2001) and the NESDIS vegetation fraction climatology. The vertical dust flux is distributed over three log-normal size modes by means of a standard error function reflecting the observed background aerosol distribution over source regions (D'Almeida, 1987; Zender et al., 2003b). These 3 bins are re-distributed over 8 transport model size bins with effective radii of 0.15, 0.25, 0.45, 0.78, 1.3, 2.2, 3.8, 7.1 µm.

The dust dry deposition is based on Zhang et al. (2001) and includes simplified empirical parameterizations for the deposition processes of Brownian diffusion, impaction, interception and gravitational settling detailed in Slinn (1982).

Wet scavenging of dust by precipitation is computed separately for convective and grid-scale precipitation. The model includes parameterizations for in-cloud and sub-cloud scavenging. The standard cloud and precipitation schemes of the NMMB model are the grid-scale cloud microphysical scheme of Ferrier et al. (2002), and the convective adjustment scheme of Betts-Miller-Janjic (BMJ) (Betts, 1986; Betts and Miller, 1986; Janjic, 1994). For moist convective mixing it is assumed that dust is mixed vertically analogously to moisture, so that the reference vertical profile for dust preserves similarity to that of moisture in the BMJ approach.

2.2 Model set-up

We performed regional simulations in a domain covering Northern Africa, the Arabian Peninsula and Southern/Central Europe (0° N to 65° N and 25° W to 55° E) as shown in Fig. 1. The model resolution was set to $1/4^\circ \times 1/4^\circ$ (about 25 km) with 40 vertical layers in the vertical for all simulations which is expected to be the regional forecast model resolution. The model meteorology was reinitialized every 24 h and the boundary conditions updated every 6 h with global NCEP final analysis (FNL) data at $1^\circ \times 1^\circ$ resolution. A seven-day dust spin-up was performed for each simulation. For the BoDEx period, we performed additional simulations using soil moisture initial conditions from the Global Land Data Assimilation System (GLDAS) (Rodell et al., 2004).

The model backscatter coefficient is derived directly from the extinction coefficient, applying an empirical extinction-to-backscatter or lidar (LR) ratio. The LR is rather

ACPD
11, 30273–30331, 2011

variable and depends strongly on particle shape (Mishchenko et al., 1997). We use a constant LR of 50 sr suggested by Papayannis et al. (2007) after conducting a statistical analysis of dust events with data from the European Aerosol Research LIdar NETwork (EARLINET). The model number size distribution is diagnosed at the corresponding height levels and is derived assuming sphericity and average dust particle density of 2.6 g cm^{-3}.

3 Observational data

This section provides a brief introduction of the two field experiments and describes the available observational in-situ and remote sensing products. In Fig. 1, the red dots refer to the SAMUM-1 field sites at Ouarzazate Airport and Tinfou/Zagora and the green and yellow dots indicate the AERONET and EARLINET stations complementary used here for the same period. The region where the Falcon overflight took place on 19 and 20 May 2006 is indicated with the red line. The blue dot refers to the BoDEx field campaign site at Chicha in the Bodélé depression. The respective station names, acronyms and locations are given in Table 1.

3.1 SAMUM-1 field experiment

SAMUM-1 took place from 11 May to 10 June 2006 in Southern Morocco, around Ouarzazate, Tinfou (720 m a.s.l.) and Zagora (situated 150 km southeast of Ouarzazate and next to Tinfou). It was accompanied by several overflights of two research aircraft (Falcon and Partenavia).

In this study, we use profiles of the 532 nm extinction coefficient from the six-wavelength aerosol lidar Backscatter Extinction lidar-Ratio Temperature Humidity profiling Apparatus (BERTHA) at Ouarzazate (Althausen et al., 2000; Tesche et al., 2009). Profiles are available for heights between 1 and 7 km and the lidar data have a temporal resolution of 30 s and a vertical resolution of 60 m. They are cut above due to a rather

ACPD
11, 30273–30331, 2011

noisy signal (Müller et al., 2009). The airborne measurements taken aboard the Falcon aircraft of the German Aerospace Center (DLR) combined HSRL (Esselborn et al., 2009) at 532 nm with extensive in-situ instruments (Weinzierl et al., 2009) to probe the atmosphere in the Ouarzazate area between the surface and 11 km height. The surface size distribution was quasi-continuously measured by means of a combination of a Differential Mobility Particle Sizer (DMPS) and an Aerodynamic Particle Sizer (APS). The mobility or aerodynamic size range was between 20 nm and 5 µm diameter, respectively (Schladitz et al., 2009). Large particles between 4 and 500 µm were collected by two different impactor types applying the method of impactor collection on coated glass substrates once every day (Kandler et al., 2009; Schladitz et al., 2009).

The upper level vertical aerosol size distribution was derived on constant altitude sequences without the presence of clouds aboard the Falcon aircraft over the Ouarzazate region (same flight as for lidar measurements). It carried instrumentation for measuring dust particle size distributions in the size range of 4 nm to 100 µm diameter using Condensation Particle Counters (CPCs) and several Optical Particle Counters (OPCs). Particles larger than 30 µm were present in ∼ 50 % of the cases (Esselborn et al., 2009; Weinzierl et al., 2009).

3.2 BoDEx field experiment

BoDEx took place from 28 February to 13 March 2005 and represents the first and unique field study in the Bodélé depression, which lies between the Tibesti mountains and Lake Chad in Mali. The observation site Chicha was located at the eastern margin of the large diatomite deposit, originating from the paleo-lake Mega-Chad. It is known to be one of the global key source areas for mineral dust (Prospero et al., 2002; Washington et al., 2003), exhibiting a pronounced dust emission hot spot (Giles, 2005; Todd et al., 2007).

Time-height profiles of wind speed and direction were derived from PIlot BALloon (PIBAL) ascents (Devara et al., 1998; Egger et al., 2005). Nine ascents were made per day with higher sampling frequency in the morning so that the effects of surface heating

ACPD
11, 30273–30331, 2011

on the wind field could be best resolved. The single theodolite method was used, with heights calculated from the balloon's buoyancy prior to release and balloon elevation and azimuths recorded at minute intervals. Wind speed and direction was averaged over 2 min intervals so that the effects of turbulent eddies could be minimized. Typical daytime tracks lasted 35 min and typical nighttime tracks lasted 18 min. Wind field with PIBALs could not be sampled in case of extreme dust events and too low visibility (Washington et al., 2006a). AOD was measured at the Chicha ground station by means of CIMEL Sun photometer and so is temperature (Todd et al., 2008b,a).

3.3 Satellite remote sensing products and data

To qualitatively compare the spatio-temporal distribution of the modeled extinction AOD, satellite based remote sensing retrievals are used. The MSG infrared dust index is an RGB (Red, Green, Blue) composite image based upon infrared channel satellite data providing the dust aerosol information by means of a pink colored contrast image. It is computed from the brightness temperature differences of three SEVIRI channels (IR 8.7, 10.8, 12.0) and is designed to monitor the evolution of dust storms and hence a useful tool to identify dust sources both at day and night (Schmetz et al., 2002). For example, a dust source activation frequency map was derived (Schepanski et al., 2007) and analyzed regarding the sub-daily distribution as a function of meteorological processes (Schepanski et al., 2009). Complementary, we use the NASA's SeaWiFS instrument that provides visible dust images (Hooker et al., 1992). It has been used in some studies to identify the dust transport (e.g. Darmenova et al., 2005; Antoine and Nobileau, 2006; Pérez et al., 2006a).

OMAERO is the standard product of the OMI sensor on board of the Aura satellite, based on the multi-wavelength UV-VIS aerosol algorithm (Levelt, 2002; Torres et al., 2007) in order to calculate AOD. The Aura platform circulates in a sun-synchronous polar orbit with a local afternoon equator crossing time at 13:45 LT, providing global coverage in one day. In this study, we use the daily level-3 AOD product at 500 nm at $1^\circ \times 1^\circ$ resolution. The data has to be treated with particular caution due to its weak

ACPD
11, 30273–30331, 2011

sensitivity to boundary layer aerosol owing to high desert surface reflectivity (Martin, 2008; Badarinath et al., 2010), or cloud contamination (Hsu et al., 1999). OMI also tends to indicate heavy biomass burning in the Sahel (Basart et al., 2009; Cavalieri et al., 2010) and it may overestimate the winter AOD relative to MISR and MODIS (Ahn et al., 2008; Zhao et al., 2010).

The MODIS instruments on board the Terra and Aqua platforms have been used extensively for global mapping of AOD. It measures backscattered solar radiation with seven wavelength bands dedicated to aerosol retrieval. MODIS AODs are most reliable over the ocean being moderately biased over arid regions (Kinne et al., 2003; Remer et al., 2005; Levy et al., 2007; Drury et al., 2008). Here we use the MODIS Deep Blue (MODIS DB) product which is based on an algorithm which uses multiple radiances (blue channels), including the 412 nm channel derived from the MODIS instrument onboard of the Aqua satellite (Hsu et al., 2004). It provides near-global daily information of optical depth at 550 nm wavelength at about 10 km resolution daily at local noon, allowing for the direct characterization of the origin of individual aerosol sources even over highly reflective sources such as deserts. Here, we use the MODIS Terra and DB level-3 AOD products at 550 nm and $1^{\circ} \times 1^{\circ}$ resolution.

3.4 Ground based measurement data

For a quantitative validation, the model-derived AOD is additionally compared with data from 7 AERONET stations. This network of sky calibrated CIMEL Sun photometers measures the direct solar radiance at eight wavelengths and sky radiance at four of these wavelengths at a daily base (Holben et al., 1998). Thereby, measurements are taken every 15 min. It provides AOD at 440 or 500 nm and Ångström exponent (440–870 nm) (Dubovik et al., 2000; Dubovik and King, 2002). For this study, level 2.0 data are used exclusively, being quality-assured and cloud-screened. Note that background aerosol might influence the retrieved values as the Sun photometer measurements represent AODs of the total aerosol column (Heinold et al., 2009). The stations used in this study are shown in Fig. 1 (yellow dots) with the location specified in Table 1. The

ACPD
11, 30273–30331, 2011

AERONET data are supplemented by AOD measurements taken during SAMUM-1 at Zagora ground station by means of Sun photometers/sky radiometers (Hoyningen-Huene et al., 2009).

Another important source of observational data is EARLINET, providing systematic lidar observations of vertical profiles over Europe on a coherent network basis. Twenty stations across Europe are deployed using elastic backscatter and Raman lidar systems to measure the vertical profiles of the aerosol backscatter and extinction coefficients at various wavelengths between 351 and 1064 nm (Bösenberg et al., 2003). The EARLINET Raman lidar systems were quality assured performing direct intercomparisons (Matthias et al., 2004; Böckmann et al., 2004). The derived data are finally stored in a central database after cloud screening. Three stations in Southern Europe are chosen for comparison during the SAMUM-1 period as specified in Fig. 1 (green dots) and Table 1.

4 Results and discussion

4.1 SAMUM-1

4.1.1 Spatial dust distribution

We focus on the period 16–21 May 2006 whose meteorological situation including the observed spatio-temporal evolution of the dust plume over North Africa and Europe is examined in Knippertz et al. (2009). Figures 2–7 display the maps of model results and satellite products for this period. For each day, we show a four hour model average AOD which coincides with the passage of the satellite over the region, i.e. between 11:00 and 15:00 UTC, the modeled surface dust concentration at 12:00 UTC, a combined map of MODIS DB (over arid and semi-arid areas) and Terra AOD (over ocean and land), the OMI AOD, the modeled 10 m wind speed, and the SeaWIFS and MSG RGB image at 12:00 UTC.

ACPD
11, 30273–30331, 2011

Satellite images outline dust source activation in Central Algeria and a pronounced dust plume over Mali, Niger and Chad on 16 May (see Fig. 2a–g). The model is generally consistent with MODIS DB over main activation spots, although these are not always precisely located. The model reproduces the dust in the Bodélé depression (Chad), at the border between Niger and Burkina Faso, mostly over Central Algeria, along the Moroccan coast and over Southern Saudi Arabia. While the model misses out the AOD over the northern part of Libya, the AOD over Northwestern Sudan is overestimated. The MSG RGB image confirms the active sources over Central Algeria, Chad, and Western Sudan. In the course of the day, the dust was advected in easterly direction towards the Moroccan coast, and driven anticyclonically along the coastline towards the Iberian Peninsula. The model captures this feature when compared to MODIS DB, SeaWIFS VIS and MSG. Over Mauritania, Algeria and Niger, OMI AOD estimates are considerably higher than the model AOD and the MODIS DB product.

On 17 May (see Fig. 3a–g), the dust advected along the Moroccan coast led to extensive dust loading over the Central and Eastern Iberian Peninsula. The modeled AOD corresponds well with MODIS DB and Terra and qualitatively matches the MSG and SeaWIFS images. Dust source activation in Chad (Bodélé) is placed correctly in the model compared with MODIS DB. The model also simulates the dust emission from Northern Sudan as visible in the MSG image. Weaker model AOD over Western Libya indicates underestimation when compared with OMI, which itself overestimates when compared with MODIS DB with weak correspondence in the MSG image. Better agreement between OMI and MSG is found in Eastern Mali, where only minor dust source activation is simulated. No clear conclusion can be drawn over the Arabian Peninsula, given the rather strong disagreement between MODIS DB and OMI AOD.

On 18 May (see Fig. 4a–g) the dust plume stretched over the Western Mediterranean Sea and Northern Italy, as indicated by the model and MODIS Terra. Dust production in Mali, Niger, Chad and Sudan is placed correctly in the model. Again, the moderate AOD over Northern Libya in the retrievals is not captured by the model.

ACPD
11, 30273–30331, 2011

Poor agreement is found between OMI and MODIS DB AOD in Mauritania, where the MSG RGB retrieval suggests moderate dust occurrence in the north (weak presence in MODIS DB only), including a stretch of heavy dust in south-central Algeria. The latter is adumbrated in the model, MODIS DB and OMI. However, AOD over Central Mauritania is clearly underestimated in the model. In turn, OMI potentially overestimates the AOD compared to MODIS DB, especially in Eastern Chad.

The dust event over Southern Europe covers the Mediterranean Sea including large portions of Italy and the Balkan Peninsula on 19 May (see Fig. 5a–g). The simulated dust pattern is consistent with MODIS DB, Terra and SeaWiFS VIS product. It is partly obscured from clouds in the MSG dust image, although identifiable along the Moroccan coast. MSG also shows dust source activation in the north and south of Mauritania, as well as in Southern Algeria, confirming the modeled surface dust concentration to a large extent. As already seen on previous days, the model liberates significant amounts of dust at the northern tip of Mauritania, corresponding fairly well with OMI AOD but not with MODIS DB.

In the late afternoon hours on 19 May (Fig. 5), an interesting synoptic evolution was observed with deep moist convection developing over North-eastern Mali. In the night of 19 to 20 May the induced precipitation due to convection and the associated evaporational cooling caused the formation of a large haboob, whose leading edge quickly spread north and westwards (Knippertz et al., 2009). OMI AOD and MSG RGB show dust mobilization mainly occurring over Mali, resulting in an large dust plume over Northern Mali, the southern tip of Algeria, Eastern Mauritania and Western Chad at noon on 20 May (see Fig. 6a–g). The model is not able to capture the intensity of the event due to an inaccurate representation of the moist convection as discussed in previous modeling studies (Haustein et al., 2009; Heinold et al., 2009) and as evident in the modeled 10 m wind speed which is rather smoothly distributed and not exceeding moderate velocity. Nonetheless, the pattern of the modeled AOD at least resembles the shape of dust plume in the DB retrieval. Over the Bodélé, the modeled AOD agrees well with MODIS DB, while the MSG dust image suggests rather low AOD values.

ACPD
11, 30273–30331, 2011

Finally, the Mediterranean dust outbreak is consistently shown by the model, SeaWIFS and OMI. Although the model fails to reproduce the intense moist convective event, dust is still liberated intensively at the leading edge of the cold pool outflow over Mauritania and Mali on 21 May (see Fig. 7a–g). As on 20 May, OMI shows a strong feedback in terms of AOD while MODIS DB is considerably less sensitive, indicating that the model reproduces the shape of the dust plume over Mauritania. Moreover, the high AOD values evident in the OMI retrieval are not fully confirmed by the MSG dust image over Eastern Mauritania in particular. The model matches also the MODIS DB AOD over the Bodélé.

4.1.2 Aerosol optical depth

In Figs. 8 and 9 we show the comparison of AOD between 8 stations (7 AERONET stations including the additional Sun photometer measurements taken during the SAMUM-1 campaign at Zagora) and NMMB/BSC-Dust for the period from 16–22 May 2006.

Ångström exponent values higher than 0.6 indicate significant influence of fine anthropogenic aerosols. For example, in Lampedusa anthropogenic aerosol was dominant on 16–18 May, while a dust event beginning on 19 May was observed and successfully simulated in the model. It also reproduces the dust AOD close to dust sources (Tamanrasset) and away from sources (Lampedusa and Palencia). Only on 16 May at Saada the model overestimates the AOD. In general there is a satisfactory agreement at Ouarzazate, Zagora and Saada stations between model and observations. Notice also, that the model simulates a weak diurnal dust cycle at Ouarzazate and Zagora. The impact of the large haboob on 20 May is not observed in the in-situ measurements due to their location. In Banizoumbou, the model overestimates the AOD, which remains rather constant at values between 0.7 and 0.8 during the period due to a persistent dust transport by trade winds from Saharan sources.

ACPD
11, 30273–30331, 2011

4.1.3 Vertical dust distribution

Data from BERTHA and HSRL lidar taken during the field campaign are complemented by EARLINET data. The location of the stations is given in Fig. 1 and Table 1. Figures 10 and 11 show measured (blue) and model-derived (brown) vertical profiles of the extinction coefficient in chronological order. Also the modeled dust load is provided. The altitude is relative to sea level and the model profiles over Ouarzazate are truncated at 1.7 km height due to model topography. The relative uncertainties provided for the HSRL lidar extinction coefficient are 8–22 % and those for the BERTHA lidar, estimated from the backscatter coefficients, are 10–20 % (Tesche et al., 2009).

As discussed in Knippertz et al. (2009), an upper-level ridge present over Northwestern Africa transported dust from Eastern and Central Algeria along the Moroccan coast towards the Iberian Pensinsula and from there further across Southern Europe to Greece where the dust plume arrived on 20 May. While high dust load is observed continuously over Ouarzazate, Saada and Zagora (see Figs. 8 and 9), it is present over Palencia on 17 May and arrives at Lampedusa on 19 May. Backward trajectories calculated on 19 May from the four Italian EARLINET stations (not shown) confirm the anticyclonic track from Western Algeria across the Iberian Peninsula (Müller et al., 2009). The dust was then prevailing over Italy and Greece. Backward trajectories calculated on 21 May from Athens and Thessaloniki show a path similar to those arriving at the Spanish and Italian stations, but the corresponding airmass is delayed by about 2 or 4 days (Müller et al., 2009).

At noon on 17 May (Fig. 10a), BERTHA indicates a well mixed planetary boundary layer (PBL) over Ouarzazate, between the surface and 5 km, which is consistent with the vertical humidity profile taken at 10:35 UTC as shown in Fig. 12a. In both lidar and radiosonde profiles, the observed mixing height (MH) at $\sim$ 4.6 km is underestimated by the model whose PBL does not show any tendency to grow before late afternoon. At lower levels between 2 and 3 km, the model overestimates the dust extinction by almost a factor of 2. Since a layered structure of the PBL was repeatedly observed

ACPD
11, 30273–30331, 2011

during the field campaign, the small secondary peak at 4.5 km height could well be an indication of a residual layer from the previous day. The layering is generated when the previous day mixed layer becomes decoupled from the surface due to nocturnal cooling and remains as residual layer until eroded by the formation of the new mixed layer (Heinold et al., 2009; Knippertz et al., 2009).

The next day at 11:00 UTC (Fig. 10b), the model exhibits a layer between 4 and 5 km height not visible in the lidar profile and overestimates the extinction at lower levels. The vertical profile over Naples at 19:00 UTC (Fig. 10c) is qualitatively captured by the model, however slightly overestimated above 3 km and mixed too high up to mid-tropospheric levels. The latter cannot be explained by strong vertical motion due to high lapse rates, since no distinct deep convection takes place in the model at that particular day. The vertical profile at 21:00 UTC over Ouarzazate (Fig. 10d) shows that the model captures the height of the dust layer, but it overestimates the BERTHA extinction coefficient by more than a factor of 2, reaching values as high as 140 $\mathrm{M\,m^{-1}}$.

On 19 May at 11:00 UTC (Fig. 10e), again the model underestimates the MH and overestimates the low level extinction due to weak vertical mixing. The model profile three hours later at 14:00 UTC (orange dashed line) better agrees with the observations and places the MH between 4 and 5 km height. As on 18 May, the comparison of the dust profiles is similar to that of the humidity profiles as (Fig. 12b,c). Note also that Fig. 12 includes complementary wind profiles (radiosonde and model) over Ouarzazate which show model overestimation close to the ground but good overall agreement at higher levels, where the wind field is not influenced by orography.

As shown for Naples on 18 May, dust towards Greece and the Eastern Mediterranean is mainly transported between 3 and 7 km altitude. The eastern edge of the dust plume reaches Thessaloniki on 20 May, as illustrated by the modeled extinction profile (Fig. 11a) with a maximum at 3 km height. Terra AOD confirms the arrival of the dust plume. However the lidar observation shows a lesser vertical extension and a lower maximum plume height. Note that higher low level extinction in the lidar profiles (first 2 km above ground) over Athens and Thessaloniki (particularly obvious in

ACPD
11, 30273–30331, 2011

Fig. 11d) are due to anthropogenic aerosols.

On 21 May at 14:00 UTC, the model strongly overestimates the dust plume in Athens (Fig. 11b). Satellite observations indicate that the dust plume had moved further south. The orange dashed line depicts the modeled vertical dust distribution at 18:00 UTC which better matches the lidar profile, and confirms a few hours of temporal mismatch. At 19:00 UTC the same day (Fig. 11c) the model captures the observed vertical distribution while the dust slowly moved south. The remaining dust can be seen over Athens at 11:00 UTC on 22 May (Fig. 11d) with a peak altitude between 2 and 3 km which is captured by the model. At lower levels the lidar signal is strongly affected by anthropogenic aerosols.

Beginning on 20 May over Morocco, a second dust event, induced by low pressure over Tunisia, Algeria and Libya and accompanied by strong southwesterly mid-level winds over the Iberian Peninsula and the Western Mediterranean, advected a plume over the Mediterranean Sea, Corsica and Sicily towards Italy, where it arrived late on 22 May. Over Naples (Fig. 11e), the model moderately overestimates the dust at ~ 3 km height. The respective dust extinction cross-section (not shown) revealed that the upwind-induced vertical transport of the dust layer at the Apennines was accelerated, what led to the advection of a thin dust plume towards the south such that it affected Naples resulting in the data mismatch. It is thus a local mesoscale phenomenon of short duration, highly influenced by the model topography.

Figure 13 shows two overflight lidar backscatter profiles measured in the morning hours of 19 and 20 May during the Falcon flight over the Ouarzazate and Zagora areas (see Fig. 1), both characterized by a well mixed structure of the dust layer (Weinzierl et al., 2009). For the evaluation of the backscatter coefficient, we assume a vertically constant LR of 50 sr although it can vary with time and height considerably (Esselborn et al., 2008; Tesche et al., 2009). The HSRL cross-section illustrates a homogeneous dust layer on 19 May, with a rather constant backscatter coefficient from the surface up to 5 km height, attributable to a well mixed turbulent PBL topped by a strong inversion. The corresponding vertical profile is shown in Fig. 10e, revealing that the model

ACPD
11, 30273–30331, 2011

slightly underestimates the height of the PBL. The same pattern is found in the model cross-section, which appears more heterogeneous with higher dust concentration in the lowermost layers. Fairly good agreement can be seen further north over the Atlas mountains, both regarding MH and stratification.

While no clouds disturb the measurements on 19 May, some cirrus cloud at 6 km height obscured the underlying aerosol layer on 20 May. Also on 20 May, the HSRL cross-section illustrates an elevated dust layer, centered at 5–6 km height to the southeast of the Atlas Mountains. Knippertz et al. (2009) suggested differential advection during the night and subsequent mixing as a possible mechanism to explain this distribution. The pronounced dust layer to the northwest of the Atlas at ∼2 km height is reproduced by the model, although overestimated. Over the mountain range, the dust is transported vertically due to mountain waves in the model. The dust layer is thicker and appears at a lower altitude than in the observations to the southeast of the Atlas. The top height of the mixed PBL at 5.5 km is well captured by the model, but the rather stratified well mixed dust layer does not match the observation. Given the moderate overestimation over the Mauritania/Morocco border region in terms of AOD in the model, too much dust is persistently transported to the southwest of the Atlas mountains compared to the satellite imagery (see Fig. 6a–c).

4.1.4 Particle number size distribution

The surface size distribution at Tinfou (from a combined DMPS and APS measurement) and the particle size distribution over Ouarzazate on 19 (11:00 UTC) and 20 May 2006 (13:00 UTC) at 3.2 km and at ∼5 km height are shown in Fig. 14a–f. On both occasions, the heights correspond with the 520 hPa and 670 hPa level in Fig.14g–k, which shows the modeled longitudinal and latitudinal dust extinction cross-sections during the overflights in order to illustrate the influence of the orography upon the modeled spatial dust distribution.

Apart from very large particles, the dust size spectra near the surface are well captured. This is also true in the free troposphere, except at 4.8 km height on 19 May,

ACPD
11, 30273–30331, 2011

when the model underpredicts the number concentration due to a low dust MH (see Fig. 10e). The MH is higher in the small band of high extinction coefficients visible at 6° E between 550 and 600 hPa in Fig. 14j, which is placed just east of the overflight track in the model. Nonetheless, the simulated size spectrum agrees with the observations on 19 and 20 May, demonstrating that the model is able to reproduce the dust particle size distribution. Very large particles at the surface are underestimated from the model since their limited atmospheric residence time prevents them from being further uplifted due to gravitational settling. This features cannot be fully resolved by the model given its vertical resolution with the first layer being representative for the lowermost 80 m in our case. The average dust particle size thus does not entirely reflect the measured surface size distribution as discussed in Haustein et al. (2009). Moreover, highly variable surface wind speeds may have affected the measurements implying uncertainties as discussed in Schladitz et al. (2009) and Kandler et al. (2009). Particles smaller than 0.2 µm in diameter are most likely not related to dust, rather than to other aerosol species (Schütz et al., 1981), thus being not considered in the model. Also, particles larger than 20 µm in diameter are not taken into account since they are not contributing to long-range transport.

4.2 BoDEx

In this section, we analyze the period 1–11 March 2005 over the Bodélé. The dust annual cycle in this region follows a semi-annual pattern with peaks in the boreal spring and fall (Washington et al., 2006a,b). The considered early spring case is characterized by days with and without dust source activation, but with generally lower emission rates than in late spring. In our case, 10 and 11 March 2005 were substantial dust emission days with strongly restricted surface visibility over the measurement site in Chicha, accompanied by other moderate events on 3–7 and 9 March (Fig. 15a). The synoptic pattern during this episode was mainly characterized by a negative March North Atlantic Oscillation (NAO) index, favoring a weak Azores anticyclone, which in turn featured a precession of low-pressure systems from southwest to northeast across

ACPD
11, 30273–30331, 2011

the Mediterranean and a blocking anticyclone west of the British Isles as observed at the beginning of the month. Between 9–12 March, the blocking anticyclone over the Northeastern Atlantic suddenly migrated eastward, extending a very strong ridge of high pressure across North Africa in the form of a redeveloped Libyan high (Washington et al., 2006a).

Several dust modeling studies have been conducted using the BoDEx dataset (e.g. Tegen et al., 2006; Bouet et al., 2007; Todd et al., 2008a). Tegen et al. (2006) tested several input parameters in their emission scheme with a box model, and compared dust emissions calculated with the observed wind speeds to those calculated with wind speeds from their regional model. On the other side, Todd et al. (2008b) compared five regional dust atmospheric models including BSC-DREAM, in terms of meteorology, dust emission and transport. Among other results, Todd et al. (2008b) reported strong near-surface wind speed underestimations, an unresolved out-of-phase relationship of the diurnal cycles of the LLJ and the surface winds in most models and an order of magnitude difference in the AOD among models.

Below we evaluate and analyze the skills of the NMMB/BSC-Dust to reproduce the meteorology and the dust patterns in this prominent dust source. We also detail the performed model experiments, which were all initialized using $1^\circ \times 1^\circ$ NCEP FNL analysis atmospheric data.

4.2.1 Surface meteorology and dust emission

Time series of modeled and observed dust AOD, 10 m wind speed and 2 m temperature for the period 1–11 March at Chicha are displayed in Fig. 15. For reference Chicha is located in Western Chad south of the Tibesti mountains (blue dot in Fig. 1).

The first model experiment (NCEP-FNL) was initialized with NCEP FNL analysis soil moisture and soil temperature fields. In this case, the comparison with observations reveals a strong AOD underestimation over the entire period, particularly on days 4, 9, and 11 (Fig. 15a). AOD measurements are not available on 10 March due to the reduced visibility associated with the heavy dust storm (Washington et al., 2006a; Todd

ACPD
11, 30273–30331, 2011

et al., 2007). On 11 March, the model underestimates the AOD peak and shows a temporal delay with respect to the observed AOD in the afternoon. As shown in Fig. 15c the model underestimates the daily maximum surface wind up to 50 % while it usually overestimates the nighttime winds. We also found a systematic cool temperature bias during the day as strong as 10 K (Fig. 15d), which suggested a poor soil moisture initialization. We tested the latter hypothesis in a second experiment (NCEP-GLDAS) by running the model using soil initial conditions from the Global Land Data Assimilation System (GLDAS) calculated with the Noah Land Surface Model (Ek et al., 2003).

In general, NCEP-GLDAS does a good job capturing the amplitude of the 2 m temperature due to a more accurate (drier) soil moisture over deserts. Zender et al. (2003a) already reported that NCEP soil moisture is usually too high over active dust emission regions all year long, which hampers its use in dust models. NCEP-GLDAS underestimates the minimum temperature on 1, 2, 10 and 11 March and the maximum temperature on 7 and 8 March. Since our simulations do not explicitly account for dust radiative effects, the high dust loading on 10 and 11 March, which should inhibit outgoing LW radiation to reach higher levels, may at least partly explain the observed nocturnal temperature difference. Also the slight overestimation of the maximum temperature on 10 March may be an indicator of the neglected dust SW radiative cooling effect in the simulation. The drier soil moisture in NCEP-GLDAS has consequences over the simulated dust by reducing the threshold wind friction velocity and slightly increasing the maximum daily wind speed with respect to NCEP-FNL (Fig. 15c). The latter is due to an increased mixing of momentum down to the ground driven by an enhanced surface sensible heat flux. In comparison to NCEP-FNL, NCEP-GLDAS shows a slightly higher dust AOD on the 9, 10 and 11 March and a significantly higher AOD on 4 March, which is closer to observations. However, the AOD underestimation remains very strong over the study period due to the underestimated winds in the model.

Tegen et al. (2006) performed simulations at 7 km resolution with a regional model. While the use of higher resolution helped developing stronger daily winds compared to our 25 km resolution simulation, the daily wind peaks remained underestimated and

ACPD
11, 30273–30331, 2011

nighttime wind speeds overestimated with respect to observations. In their study, the use of a Weibull probability distribution to account for sub-gridscale variability of surface winds resulted in a better AOD agreement over the 3–7 March period, but also in an unrealistically high AOD (above 100) for the 9–11 period.

Motivated by the shortcoming of the model to reproduce the maximum surface wind speeds at this resolution, observed particularly on 5–7 and 9 March, we conducted three additional experiments. First, we increased the horizontal-to-vertical-flux-ratio (α) in the emission scheme by a factor that minimized the AOD model error. In our model we follow an empirical relationship by which the vertical dust flux is proportional to the horizontal sand flux. α is the coefficient of proportionality reflecting the availability of dust in the soil, which is calculated as the sum of the vertical to horizontal flux ratio of each soil population class weighed by their mass fraction in the soil (Pérez et al., 2011). α in the model for the Bodélé is estimated to be $3.6 \times 10^{-6}\,\mathrm{cm}^{-1}$. In this experiment we multiply α by 1.605, the factor which gives lowest bias in comparison with Sun photometer AOD. In two other experiments we reduced the threshold friction velocity by 30 and 50 %, which is approximately the range of underestimation when we compare the modeled and observed diurnal wind speeds. The results are displayed in Fig. 15b. On 4 March, the three experiments overestimated the AOD in the morning hours. As expected, all three experiments are generally closer to the observations over the rest of the period. In particular, the reduction of the threshold friction velocity by 50 % significantly helps reducing the bias of the model on the period 5–9 March. Also, the model emits more dust on 10 and 11 March in the three experiments. However, the delay of the model on 11 March hampers any definite conclusion about the modeled intensity for this event.

In Fig. 16a–c we show model and satellite dust distributions centered over the Bodélé for 4, 10 and 11 March. As expected, MODIS DB (Fig. 16d) places the highest AOD over the Bodélé and features significant dust activity in surrounding regions. The model captures qualitatively many of the dust patterns observed from the satellite observations. The differences among the model experiments are mainly quantitative and there

ACPD
11, 30273–30331, 2011

are no remarkable differences in the qualitative patterns. The improvements achieved by increasing the value of alpha or reducing the threshold friction velocity are also confirmed by comparison with satellite data.

The model clearly captures the shape and extent of the main dust plume emitted from the Bodélé. On 4 March the model reproduces the dust activity in Southern Libya, Northern Chad and Nigeria visible in the satellite maps. The model does not show much of the freshly emitted dust from Eastern Sudan as clearly visible in the MSG RGB product (Fig. 16e). The significant dust load in Niger highlighted in MODIS DB is not represented in the model. This roughly coincides with the presence of clouds in the MSG RGB product, which suggests cloud contamination in the MODIS DB AOD retrieval. On 10 and 11 March very high AOD values are present over the the Bodélé. On 10 March the model captures the extent of the Bodélé dust plume and reproduces the dust activity in Northern Niger close to the border with Chad and Libya and in the intersection with Algeria and Mali. On 11 March, MODIS DB and MSG RGB indicate that the dust plume extends further south as far as Cameroon and Nigeria. The model agrees well in both days, only significantly underpredicting the AOD over Southwestern Niger on 11 March.

4.2.2 Bodélé Low Level Jet

The Bodélé Depression is dominated by the northeasterly Harmattan winds of North Africa in all months except July and August, when the intertropical convergence zones moves sufficiently far north to bring light and variable winds over the Bodélé (Washington et al., 2006a). This northeasterly winds are likely to be accelerated between the Tibesti and Ennedi massifs (Koren and Kaufman, 2004), supporting a pronounced easterly LLJ, evident also in the wind data from NCEP reanalysis with maximum wind speeds at 925 hPa overlying the Bodélé area (Washington and Todd, 2005; Todd et al., 2008b) (not shown). Usually, this LLJ feature is clearly present until May, when it is partly superimposed and weakened by the African Easterly Jet over the Sahel. It is absent to the west and weakens to the south. It disappears south of 10° N and north

ACPD
11, 30273–30331, 2011

of 22° N as described by Washington and Todd (2005). During the BoDEx campaign, the Bodélé LLJ with its pronounced diurnal cycle was evident under dusty as well as dust-free conditions (Washington et al., 2006a). Wind speeds are at maximum in the midmorning hours with calm conditions at night when the vertical turbulent flux is at minimum due to absent surface heating. Although wind was peaking at 10 m s^{-1} at dust-free days, it was not high enough to cause dust deflation. At dusty days, the amplitude of the diurnal cycle was similar to dust-free days but with winds speeds peaking well above 14 m s^{-1}. According to Washington et al. (2006a), the corresponding wind speed threshold coinciding with deflation, suspension and saltation of dust is 12 m s^{-1}. Winds in excess of 12 m s^{-1} were observed during the Bodélé dust outbreak between 9–12 March.

In Fig. 17, the temporal evolution of the vertical wind profile over Chicha is shown as measured from PIBAL (a), derived from NCEP FNL analysis (b) and simulated from the model with NCEP FNL atmospheric analysis and GLDAS soil conditions (c). While NCEP reanalysis data intrinsically underestimates the surface wind during daytime hours by more than 60 % at occasions (Koren and Kaufman, 2004; Todd et al., 2008b), the NCEP analysis underestimation of the low level wind is still more than 50 % (see Fig. 17b). The poor resolution of the diurnal wind cycle is probably due to difficulties of the NCEP model to resolve smaller boundary layer features at the given vertical and spatial resolution. Taking into account the clear underestimation of the vertical NCEP wind field, the model reproduces the observed wind speeds surprisingly well. Although lower, the model peak winds of approximately 20 m s^{-1} are much closer to the observed wind maxima which reach wind speeds in excess of 24 m s^{-1} at night. The general pattern – with highest wind speeds observed on 4 March and during the Bodélé dust outbreak – is well reproduced with some underestimation on 6 and 7 March. The midmorning Bodélé LLJ is captured not only in its vertical extension but also regarding the diurnal temporal evolution. However, as shown at the surface, the model misses the peak wind speeds mostly on 5–7 and 9 March. Apart from the weaker LLJ at those days, the PIBAL data also suggest that the potential momentum

ACPD
11, 30273–30331, 2011

provided by the LLJ was not transported down to the surface. However, it is effectively mixed down by turbulence especially on 4, 10 and 11 March, consistent with modeled surface wind speeds (compare Fig. 16). At 25 km resolution, the model reproduces the typical LLJ over the Bodélé and satisfactorily simulates the diurnal wind cycle at the surface, although it underestimates the peak wind velocities at days with moderate average wind speeds.

5 Conclusions

In the companion paper (Pérez et al., 2011), we described the new NMMB/BSC-Dust model and we presented a general evaluation of the model at global and regional scales for years 2000 and 2006, respectively. In this paper we have evaluated and analyzed in detail the behavior of the model making use of the data provided by two of the most important and recent dust experimental campaigns in Northern Africa. All the simulations presented in this contribution were run at 25 km resolution, which is expected to be the standard model resolution for dust forecasting at BSC.

For the SAMUM-1 campaign we examined the model's capability to reproduce the dust spatial and vertical distribution, and the dust size spectra at different height levels. For the BoDEx campaign, we focused on the model behavior to represent the meteorology and the dust patterns in the Bodélé depression, which is probably the most prolific dust source on Earth.

For the SAMUM-1 period (16–21 May 2006), the model describes fairly well the general dust patterns in Northern Africa. On 19 May, the strong dust deflation triggered by deep moist convection developed over Mali and Mauritania is, to a large extent, not reproduced by the model. The transport path towards Europe and the Mediterranean is in good qualitative agreement particularly with MODIS DB. Inefficient dust sources are identified over Eastern Mauritania and portions of Central Niger, even though the surface wind seems to be higher than the threshold friction velocity required for dust deflation. As discussed in (Pérez et al., 2011), the topographic preferential source

ACPD
11, 30273–30331, 2011

map used in the model does not reflect the Mali/Mauritania border source leading to underestimation of the emissions in that region. A more exhaustive analysis regarding the dust sources in the model will be the object of a forthcoming study. Close to the Sahel, disagreement between OMI and MODIS DB AOD hampers the validation of the model. OMI generally tends to provide higher AOD values than MODIS DB.

The AERONET comparison during the SAMUM-1 period reveals that the model reproduces the dust quantitatively well close to the sources. For this period, we found a weak daily cycle close to dust sources (Ouarzazate, Zagora), rather constant values in the Sahel (Banizoumbou) and north of the main sources regions (Tamanrasset), and dust long-range transport to Europe (Palencia) and the Mediterranean (Lampedusa) associated with distinguished dust episodes. The comparison with lidars revealed model deficiencies in the vertical distribution. We found temporal disagreement in two cases, strong overestimation in one case and mismatch regarding the MH in another four cases, particularly over Ouarzazate on 17 and 18 May. The latter is related with the PBL simulated by the model, which shows equal mismatch when comparing the observed WV mixing ratio profile (radiosonde data) and the modeled profile of the specific humidity. The difficult orographic situation over Ouarzazate and its proximity to downstream sources may introduce considerable modeling errors. Also the initial conditions, particularly in the soil may explain the insufficient mixing in Ouarzazate.

The particle number size distribution is well captured by the model, although large particles remain underestimated. Nonetheless, the simulated size spectra agrees well with the observations, at the surface as well as at 3 and 5 km altitude.

We performed several model experiments for the BoDEx period between 1–11 March 2005. We showed the importance of accurate initial soil moisture conditions in the model to reproduce the amplitude of the 2 m temperature and to better represent the intensity of the diurnal winds in the model. NCEP FNL analysis underestimates the soil water content which led to a substantial cold bias of up to 10 K. When using GLDAS soil moisture data to initialize the model, the diurnal surface temperature range is consistently reproduced with a positive effect upon dust emission over the Bodélé.

ACPD
11, 30273–30331, 2011

At the working resolution of 25 km, the model underestimates up to 50 % the daily maximum wind speed and thus significantly underestimates the dust emission and AOD. However, the persistent dust source activation period peaking over the Bodélé on 10 and 11 March is simultaneously shown by the model and the satellite retrievals. Additional experiments with an increased vertical to horizontal flux ratio or a reduction of the threshold friction velocity up to 50 % significantly improved the skills of the model.

The wind speed over the Bodélé was evaluated with specific regard to the typical wind pattern which features a persistent diurnal cycle with peak wind velocity between 500 m and 1 km above ground in the late morning hours: the Bodélé LLJ which was measured during BoDEx with the PIBAL sonde. NMMB/BSC-Dust succeeds to place the maximum wind field correctly in terms of vertical extension and temporal development. Highest wind speeds measured with the PIBAL sonde on 4 and 9–11 March correspond well with maximum wind speeds simulated by the model, showing that the model reproduces the Bodélé LLJ.

Acknowledgements. The authors would like to thank the AERONET program for establishing and maintaining the used sites. We would like to thank the EARLINET program for providing and analyzing the lidar data. We would also like to express our thanks to the whole SAMUM-1 and BoDEx team, who provided in-situ and surface based data gathered during the field campaign. In particular, we thank D. Müller, M. Tesche, M. Esselborn, B. Weinzierl, A. Schladitz and W. von Hoyningen-Huene for their lidar, impactor and meteorology data. OMI and MODIS daily data used in this paper were produced with the Giovanni online data system, developed and maintained by the NASA GES DISC. This work was developed under the research projects CGL2006-11879, CGL2008-02818, CGL2010-19652 and CSD00C-06-08924 of the Spanish Ministry of Science and Technology. Simulations were performed with the Marenostrum Supercomputer in BSC.

References

Ahn, C., Torres, O., and Bhartia, P. K.: Comparison of ozone monitoring instrument UV aerosol products with aqua/moderate resolution imaging spectroradiometer and multiangle

ACPD
11, 30273–30331, 2011

imaging spectroradiometer observations in 2006, J. Geophys. Res., 113, D16S27, doi:10.1029/2007JD008832, 832, 2008. 30284
Althausen, D., Müller, D., Ansmann, A., Wandinger, U., Hube, H., Clauder, E., and Zörner, S.: Scanning 6-wavelength 11-channel aerosol lidar, J. Atmos. Ocean. Tech., 17, 1469–1482, 2000. 30281
Antoine, D. and Nobileau, D.: Recent increase of Saharan dust transport over the Mediterranean Sea, as revealed from ocean color satellite (SeaWiFS) observations, J. Geophys. Res., 111, D12214, doi:10.1029/2005JD006795, 795, 2006. 30283
Arakawa, A. and Lamb, V. R.: Computational design of the basic dynamical processes of the UCLA general circulation model, Methods Comput. Phys., 17, 173–265, 1977. 30278
Badarinath, K., Kharol, S. K., Kaskaoutis, D. G., Sharma, A. R., Ramaswamy, V., and Kambezidis, H. D.: Long-range transport of dust aerosols over the Arabian Sea and Indian region – a case study using satellite data and ground-based measurements, Global Planet. Change, 72, 164–181, 2010. 30284
Bagnold, R. A.: The Physics of Blown Sand and Desert Dunes, Methuen, New York, 1941. 30279
Basart, S., Pérez, C., Cuevas, E., Baldasano, J. M., and Gobbi, G. P.: Aerosol characterization in Northern Africa, Northeastern Atlantic, Mediterranean Basin and Middle East from direct-sun AERONET observations, Atmos. Chem. Phys., 9, 8265–8282, doi:10.5194/acp-9-8265-2009, 2009. 30284
Betts, A. K.: A new convective adjustment scheme. Part 1: Observational and theoretical basis, Q. J. Roy. Meteorol. Soc., 112, 307, doi:10.1002/qj.49711247307, 1986. 30280
Betts, A. K. and Miller, M. J.: A new convective adjustment scheme, Part II: Single column tests using GATE wave, BOMEX, ATEX and arctic air-mass data sets, Q. J. Roy. Meteorol. Soc., 112, 308, doi:10.1002/qj.49711247, 1986. 30280
Böckmann, C., Wandinger, U., Ansmann, A., Bösenberg, J., Amiridis, V., Boselli, A., Delaval, A., De Tomasi, F., Frioud, M., Grigorov, I., Hägärd, A., Horvat, M., Iarlori, M., Komguem, L., Kreipl, S., Larchevêque, G., Matthias, V., Papayannis, A., Pappalardo, G., Rocadenbosch, F., Rodrigues, J. A., Schneider, J., Shcherbakov, V., and Wiegner, M.: Aerosol lidar intercomparison in the framework of the EARLINET project. 2. Aerosol backscatter algorithms, Appl. Opt., 43, 977–989, 2004. 30285
Bösenberg, J., Matthias, V., Amodeo, A., Amoiridis, V., Ansmann, A., Baldasano, J. M., Balin, I., Balis, D., Böckmann, C., Boselli, A., Carlsson, G., Chaikovsky, A., Chourdakis, G., Com-

ACPD
11, 30273–30331, 2011

eron, A., De Tomasi, F., Eixmann, R., Freudenthaler, V., Giehl, H., Grigorov, I., Hagard, A., Iarlori, M., Kirsche, A., Kolarov, G., Kolarev, L., Komguem, G., Kreipl, S., Kumpf, W., Larcheveque, G., Linné, H., Matthey, R., Mattis, I., Mekler, A., Mironova, I., Mitev, V., Mona, L., Müller, D., Music, S., Nickovic, S., Pandolfi, M., Papayannis, A., Pappalardo, G., Pelon, J., Perez, C., Perrone, R. M., Persson, R., Resendes, D. P., Rizi, V., Rocadenbosch, F., Rodrigues, J. A., Sauvage, L., Schneidenbach, L., Schumacher, R., Shcherbakov, V., Simeonov, V., Sobolewski, P., Spinelli, N., Stachlewska, I., Stoyanov, D., Trickl, T., Tsaknakis, G., Vaughan, G., Wandinger, U., Wang, X., Wiegner, M., Zavrtanik, M., and Zerefos, C.: EARLINET: A European Aerosol Research Lidar Network, MPI-Report, Max-Planck-Institut für Meteorologie, Hamburg, Germany, 348, 1–191, 2003. 30285

Bouet, C., Cautenet, G., Washington, R., Todd, M. C., Laurent, B., Marticorena, B., and Bergametti, G.: Mesoscale modeling of aeolian dust emission during the BoDEx 2005 experiment, Geophys. Res. Lett., 34, L07812, doi:10.1029/2006GL029184, 184, 2007. 30277, 30294

Cavalieri, O., Cairo, F., Fierli, F., Di Donfrancesco, G., Snels, M., Viterbini, M., Cardillo, F., Chatenet, B., Formenti, P., Marticorena, B., and Rajot, J. L.: Variability of aerosol vertical distribution in the Sahel, Atmos. Chem. Phys., 10, 12005–12023, doi:10.5194/acp-10-12005-2010, 2010. 30284

Christensen, J. H.: The Danish eulerian hemispheric model – a three-dimensional air pollution model used for the Arctic, Atmos. Environ., 31, 4169–4191, doi:10.5194/acp-10-12005-2010, 1997. 30276

D'Almeida, G. A.: On the variability of desert aerosol radiative characteristics, J. Geophys. Res., 92, 3017–3026, 1987. 30280

Darmenova, K., Sokolik, I. N., and Darmenov, A.: Characterization of east Asian dust outbreaks in the spring of 2001 using ground-based and satellite data, J. Geophys. Res., 110(D02204), 842, doi:10.1029/2004JD004842, 2005. 30283

Devara, P. C., Pandithurai, G., Raj, P. E., Maheskumar, R. S., and Dani, K. K.: Atmospheric aerosol-cloud-stability relationship as observed with optical and radio remote sensing techniques, Atmos. Res., 49, 65–76, 1998. 30282

Drury, E. E., Jacob, D. J., Wang, J., Spurr, R. J. D., and Chance, K. V.: Improved algorithm for MODIS satellite retrievals of aerosol optical depths over Western North America, J. Geophys. Res., 113(D16204), 573, doi:10.1029/2006GL029184, 2008. 30284

Dubovik, O. and King, M. D.: A flexible inversion algorithm for retrieval of aerosol optical properties from Sun and sky radiance measurements, J. Geophys. Res., 105, 20673–20696, 2002.

ACPD
11, 30273–30331, 2011

30284
Dubovik, O., Smirnov, A., Holben, B. N., King, M. D., Kaufman, Y. J., Eck, T. F., and Slutsker, I.: Accuracy assessments of aerosol optical properties retrieved from Aerosol Robotic Network (AERONET) Sun and Sky radiance measurements, J. Geophys. Res., 105(D8), 9791–9806, 2000. 30284
Egger, J., Blacutt, L., Ghezzi, F., Heinrich, R., Kolb, P., Lämmlein, S., Leeb, M., Mayer, S., Palenque, E., Reuder, J., Schäper, W., Schween, J., Torrez, R., and Zaratti, F.: Diurnal circulation of the Bolivian Altiplano. Part I: Observations, Mon. Weather Rev., 133(4), 911–924, 2005. 30282
Ek, M. B., Mitchell, K. E., Lin, Y., Rogers, E., Grunmann, P., Koren, V., Gayno, G., and Tarpley, J. D.: Implementation of Noah land surface model advances in the National Centers for Environmental Prediction operational mesoscale Eta model, J. Geophys. Res., 108(D22), 8851, doi:10.1029/2002JD003296, 2003. 30295
Esselborn, M., Wirth, M., Fix, A., Tesche, M., and Ehret, G.: Airborne high spectral resolution lidar for measuring aerosol extinction and backscatter coefficients, Appl. Opt., 47(3), 346–358, 2008. 30291
Esselborn, M., Wirth, M., Fix, A., Weinzierl, B., Rasp, K., Tesche, M., and Petzold, A.: Spatial distribution and optical properties of Saharan dust observed by airborne high spectral resolution lidar during SAMUM 2006, Tellus B, 61, 131–143, 2009. 30282
Fécan, F., Marticorena, B., and Bergametti, G.: Parameterization of the increase of the aeolian erosion threshold wind friction velocity due to soil moisture for arid and semi-arid areas, Ann. Geophys., 17, 149–157, 1999, http://www.ann-geophys.net/17/149/1999/. 30279
Fels, S. B. and Schwarzkopf, M. D.: The simplified exchange approximation – a new method for radiative transfer calculations, J. Atmos. Sci., 32(7), 1475–1488, 1975. 30279
Ferrier, B. S., Jin, Y., Lin, Y., Black, T., Rogers, E., and DiMego, G.: Implementation of a new grid-scale cloud and precipitation scheme in the NCEP Eta Model, in: Proceedings of the 15th Conference on Numerical Weather Prediction, pp. 280–283, San Antonio, TX, 12–16 August, 2002. 30280
Giles, J.: The dustiest place on Earth, Nature, 434, 816–819, 2005. 30282
Ginoux, P., Chin, M., Tegen, I., Prospero, J. M., Holben, B., Dubovik, O., and Lin, S.-J.: Sources and distribution of dust aerosols simulated with the GOCART model, J. Geophys. Res., 106(D17), 20255–20273, 2001. 30280

ACPD
11, 30273–30331, 2011

Haustein, K., Pérez, C., Baldasano, J. M., Müller, D., Tesche, M., Schladitz, A., Esselborn, M., Weinzierl, B., Kandler, K., and Hoyningen-Huene, W. V.: Regional dust model performance during SAMUM 2006, Geophys. Res. Lett., 36(L03812), 463, doi:10.1029/2008GL036463, 2009. 30276, 30277, 30287, 30293

Heinold, B., Tegen, I., Esselborn, M., Kandler, K., Knippertz, P., Müller, D., Schladitz, A., Tesche, M., Weinzierl, B., Ansmann, A., Althausen, D., Laurent, B., Petzold, A., and Schepanski, K.: Regional Saharan dust modelling during the SAMUM 2006 campaign, Tellus B, 61, 307–324, 2009. 30277, 30284, 30287, 30290

Heintzenberg, J.: The SAMUM-1 experiment over Southern Morocco: overview and introduction, Tellus B, 61, 2–11, 2009. 30277

Helmert, J., Heinold, B., Tegen, I., Hellmuth, O., and Wendisch, M.: On the direct and semidirect effects of Saharan dust over Europe: a modeling study, J. Geophys. Res., 112, D13208, doi:10.1029/2006JD007444, 2007. 30276

Holben, B. N., Eck, T. F., Slutsker, I., Tanre, D., Buis, J. P., Setzer, A., Vermote, E., Reagan, J. A., Kaufman, Y. J., Nakajima, T., Lavenu, F., Jankowiak, I., and Smirnov, A.: AERONET – a federated instrument network and data archive for aerosol characterization – an overview, Remote Sens. Environ., 66, 1–16, 1998. 30284

Hooker, S. B., Esaias, W. E., Feldman, G. C., Gregg, W. W., and McClain, C. R.: An overview of SeaWiFS and ocean colour, Tech. rep., NASA Technical Memorandum 104566; NASA Goddard Space Flight Center, Greenbelt, MD, 1992. 30283

Houghton, J. T., Ding, Y., Griggs, D. J., Noguer, M., van der Linden, P. J., and Xiaosu, D.: Climate Change 2001: The Scientific Basis: Contributions of Working Group I to the Third Assessment Report of the Intergovernmental Panel on Climate Change, Tech. rep., Cambridge University Press, Cambridge, United Kingdom and New York, NY, USA, 2001. 30276

Hoyningen-Huene, W. V., Dinter, T., Kokhanovsky, A. A., Burrows, J. P., Wendisch, M., Bierwirth, E., Müller, D., and Diouri, M.: Measurement of desert dust optical characteristic at Porte au Sahara during SAMUM 2006, Tellus B, 61, 206–215, 2009. 30285

Hsu, N. C., Herman, J. R., Torres, O., Holben, B. N., Tanre, D., Eck, T. F., Smirnov, A., Chatenet, B., and Lavenu, F.: Comparisons of the TOMS aerosol index with Sun-photometer aerosol optical thickness: results and applications, J. Geophys. Res., 104, D6, 6269–6279, 1999. 30284

Hsu, N. C., Tsay, S.-C., King, M., and Herman, J. R.: Aerosol properties over bright-reflecting source regions, IEEE T. Geosci. Remote Sens., 42, 557–569, 2004. 30284

ACPD
11, 30273–30331, 2011

IPCC: Climate Change 2007: The Physical Science Basis; 4th Assessment Report, Cambridge University Press, Cambridge, New York, 2007. 30276
Iversen, J. D. and White, B. R.: Saltation threshold on Earth, Mars and Venus, Sedimentology, 29, 111–119, 1982. 30279
Janjic, Z., Black, T., Pyle, M., Chuang, H.-Y., Rogers, E., and DiMego, G.: High resolution applications of the WRF NMM, in: Joint Session 16 (pp. 1–21), 17th Conference on Numerical Weather Prediction, 31 July–5 August 2005, Washington, DC, 2005. 30277
Janjic, Z., Gall, R., and Pyle, M. E.: Scientific Documentation for the NMM Solver, Tech. rep., NCAR, Boulder, Colorado, USA, 2010. 30278
Janjic, Z., Janjic, T., and Vasic, R.: A class of conservative fourth-order advection schemes and impact of enhanced formal accuracy on extended-range forecasts, Mon. Weather Rev., 139, 1556–1568, 2011. 30277, 30278
Janjic, Z. I.: The step-mountain coordinate: physical package, Mon. Weather Rev., 118, 1429–1443, 1990. 30278
Janjic, Z. I.: The step-mountain eta coordinate model: further developments of the convection, viscous sublayer, and turbulence closure schemes, Mon. Weather Rev., 122, 927–945, 1994. 30278, 30280
Janjic, Z. I.: A nonhydrostatic model based on a new approach, Meteorol. Atmos. Phys., 82, 271–285, 2003. 30278
Janjic, Z. I. and Black, T.: From global to mesoscales with a unified model, Tech. rep., National Centers for Environmental Prediction (NCEP), ams.confex.com/ams/pdfpapers/93731.pdf 2006. 30278
Janjic, Z. I. and Black, T.: A unified model approach from meso to global scales, Geophys. Res. Abstr., 9, 05025, 2007, SRef-ID: 1607–7962/gra/EGU2007-A-05025, 2007. 30277
Janjic, Z. I., Gerrity Jr., J. P., and Nickovic, S.: An alternative approach to nonhydrostatic modeling, Mon. Weather Rev., 129, 1164–1178, 2001. 30278
Kallos, G., Nickovic, S., Papadopoulos, A., Jovic, D., Kakaliagou, O., Misirlis, N., Boukas, L., Mitikou, N., Sakelaridis, G., Papageorgiou, J., Anadranistakis, E., and Manousakis, M.: The Regional Weather Forecasting System SKIRON: An Overview, in: Proc. of the Symposium on Regional Weather Prediction on Parallel Computer Environments, 1, 109–123, International Symposium on Regional Weather Prediction on Parallel Computer Environments, University of Athens, Athens, Greece, 15–17 October 1997, 1997. 30276
Kandler, K., Schütz, L., Deutscher, C., Hofmann, H., Jäckel, S., Knippertz, P., Lieke, K.,

ACPD
11, 30273–30331, 2011

Massling, A., Schladitz, A., Weinzierl, B., Zorn, S., Ebert, M., Jaenike, R., Petzold, A., and Weinbruch, S.: Size distribution, mass concentration, chemical and mineralogical composition and derived optical parameters of the boundary layer aerosol at Tinfou, Morocco, during SAMUM 2006, Tellus B, 61, 32–50, 2009. 30282, 30293

Kinne, S., Lohmann, U., Feichter, J., Schulz, M., Timmreck, C., Ghan, S., Easter, R., Chin, M., Ginoux, P., Takemura, T., Tegen, I., Koch, D., Herzog, M., Penner, J., Pitari, G., Holben, B., Eck, T., Smirnov, A., Dubovik, O., Slutsker, I., Tanre, D., Torres, O., Mishchenko, M., Geogdzhayev, I., Chu, D. A., and Kaufman, Y.: Monthly averages of aerosol properties: a global comparison among models, satellite data, and AERONET ground data, J. Geophys. Res., 108(D20), 4634, doi:10.1029/2001JD001253, 2003. 30284

Knippertz, P., Ansmann, A., Althausen, D., Müller, D., Tesche, M., Bierwirth, E., Dinter, T., Müller, T., Hoyningen-Huene, W. V., Schepanski, K., Wendisch, M., Heinold, B., Kandler, K., Petzold, A., Schütz, L., and Tegen, I.: Dust mobilization and transport in the Northern Sahara during SAMUM 2006. A meteorological overview, Tellus B, 61, 12–31, 2009. 30285, 30287, 30289, 30290, 30292

Koren, I. and Kaufman, Y. J.: Direct wind measurements of Saharan dust events from Terra and Aqua satellites, Geophys. Res. Lett., 31(L06122), 338, doi:10.1029/2003GL019338, 2004. 30297, 30298

Lacis, A. A. and Hansen, J. E.: A parameterization for the absorption of solar radiation in the Earth's atmosphere, J. Atmos. Sci., 31, 118–133, 1974. 30279

Laurent, B., Marticorena, B., Bergametti, G., Léon, J. F., and Mahowald, N. M.: Modeling mineral dust emissions from the Sahara desert using new surface properties and soil database, J. Geophys. Res., 113(D14218), 484, doi:10.1029/2007JD009, 2008. 30279

Levelt, R. F.: OMI Algorithm Theoretical Basis Document Volume 1: OMI Instrument, Level 0–1b processor, calibration and operations, Tech. rep., NASA Goddard Space Flight Center, Greenbelt, MD, 2002. 30283

Levy, R. C., Remer, L. A., and Dubovik, O.: Global aerosol optical properties and application to Moderate Resolution Imaging Spectroradiometer aerosol retrieval over land, J. Geophys. Res., 112(D13210), 815, doi:10.1029/2006JD007, 2007. 30284

Marticorena, B. and Bergametti, G.: Modeling the atmospheric dust cycle: 1. Design of a soil-derived dust emission scheme, J. Geophys. Res., 100(D8), 16415–16430, 1995. 30279

Martin, R. V.: Satellite remote sensing of surface air quality, Atmos. Environ., 42(34), 7823–7843, 2008. 30284

ACPD
11, 30273–30331, 2011

Matthias, V., Freudenthaler, V., Amodeo, A., Balin, I., Balis, D., Bösenberg, J., Chaikovsky, A., Chourdakis, G., Comeron, A., Delaval, A., De Tomasi, F., Eixmann, R., Hagard, A., Komguem, L., Kreipl, S., Matthey, R., Rizi, V., Rodrigues, J. A., Wandinger, U., and Wang, X.: Aerosol lidar intercomparison in the framework of the EARLINET project. 1. Instruments, Appl. Opt., 43, 961–976, 2004. 30285

Menut, L., Schmechtig, C., and Marticorena, B.: Sensitivity of the sandblasting flux calculations to the soil size distribution accuracy, J. Atmos. Ocean. Tech., 22, 1875–1884, 2005. 30276

Miller, R. L., Perlwitz, J., and Tegen, I.: Feedback upon dust emission by dust radiative forcing through the planetary boundary layer, J. Geophys. Res., 109(D24209), 912, doi:10.1029/2004JD004, 2004. 30276

Mishchenko, M. I., Travis, L. D., Kahn, R. A., and West, R. A.: Modeling phase functions for dustlike tropospheric aerosols using a shape mixture of randomly oriented polydisperse spheroids, J. Geophys. Res., 102(D14), 16831–16847, 1997. 30281

Mlawer, E. J., Taubman, S. J., Brown, P. D., Iacono, M. J., and Clough, S. A.: Radiative transfer for inhomogeneous atmospheres: RRTM, a validated correlated-k model for the longwave, J. Geophys. Res., 102(D14), 16663–16682, 1997. 30279

Morcrette, J.-J., Beljaars, A., Benedetti, A., Jones, L., and Boucher, O.: Sea-salt and dust aerosols in the ECMWF IFS model, Geophys. Res. Lett., 35(L24813), 041, doi:10.1029/2008GL036, 2008. 30276

Müller, D., Althausen, D., Ansmann, A., Arboledas, L., Balis, D., Comeron, A., Freudenthaler, V., Giannakaki, E., Heese, B., Heinold, B., Iarlori, M., Knippertz, P., Lopéz Marquéz, M., Marmouri, R., Mona, L., Papayannis, A., Pappalardo, G., Pérez, C., Perrone, R.-M., Pisani, G., Rizi, V., Sicard, M., Tartufo, A., Tegen, I., and Tesche, M.: EARLINET observations of the 14–22 May long-range dust transport event during SAMUM 2006: validation of results from dust transport modelling, Tellus B, 61, 325–339, 2009. 30277, 30282, 30289

Myhre, G., Berntsen, T. K., Haywood, J. M., Sundet, J. K., Holben, B. N., Johnsrud, M., and Stordal, F.: Modeling the solar radiative impact of aerosols from biomass burning during the Southern African regional Science Initiative (SAFARI-2000) experiment, J. Geophys. Res., 108(D13), 8501, 2003. 30276

Nickovic, S., Kallos, G., Papadopoulos, A., and Kakaliagou, O.: A model for prediction of desert dust cycle in the atmosphere, J. Geophys. Res., 106(D16), 18113–18129, 2001. 30276

Otto, S., Bierwith, E., Weinzierl, B., Kandler, K., Esselborn, M., Tesche, M., Schladitz, A., Wendisch, M., and Trautmann, T.: Solar radiative effects of a Saharan dust plume observed

ACPD
11, 30273–30331, 2011

during SAMUM assuming spheroidal model particles, Tellus B, 61, 270–296, 2009. 30277
Otto, S., Trautmann, T., and Wendisch, M.: On realistic size equivalence and shape of spheroidal Saharan mineral dust particles applied in solar and thermal radiative transfer calculations, Atmos. Chem. Phys., 11, 4469–4490, doi:10.5194/acp-11-4469-2011, 2011. 30277
Papanastasiou, D. K., Poupkou, A., Katragkou, E., Amiridis, V., Melas, D., Mihalopoulos, N., Basart, S., Pérez, C., and Baldasano, J. M.: An assessment of the efficiency of dust regional modelling to predict Saharan dust transport episodes, Adv. Meteorol., 2010, ID154368, 9 pp., doi:10.1155/2010/154368, 2010. 30276
Papayannis, A., Amiridis, V., Mona, L., Tsaknakis, G., Balis, D., Bösenberg, J., Chaikovsky, A., de Tomasi, F., Grigorov, I., Mattis, I., Mitev, V., Müller, D., Nickovic, S., Pérez, C., Pietruczuk, A., Pisani, G., Ravetta, F., Rizi, V., Sicard, M., Trickl, T., Wiegner, M., and Gerding, M.: Systematic lidar observations of aerosol optical properties during Saharan dust intrusions over Europe, in the frame of EARLINET (2000–2002): statistical analysis and results, J. Geophys. Res., 113(D10204), 1–17, 2007. 30276, 30281
Pérez, C., Nickovic, S., Baldasano, J. M., Sicard, M., Rocadenbosch, F., and Cachorro, V. E.: A long Saharan dust event over the Western Mediterranean: Lidar, Sun photometer observations, and regional dust modeling, J. Geophys. Res., 111(D15214), 579, doi:10.1029/2005JD006, 2006a. 30283
Pérez, C., Nickovic, S., Pejanovic, G., Baldasano, J. M., and Özsoy, E.: Interactive dust-radiation modeling: a step to improve weather forecasts, J. Geophys. Res., 111(D16206), 717, doi:10.1029/2005JD006, 2006b. 30276
Pérez, C., Jiménez-Guerrero, P., Jorba, O., Baldasano, J., Cuevas, E., Nickovic, S., and Querol, X.: Long-term simulations (1958–2006) of Saharan dust over the Mediterranean and the Eastern North Atlantic with the DREAM regional dust model, in: XXIV International Union of Geodesy and Geophysics (IUGG) General Assembly, Perugia, Italy, 2–13 July, 2007. 30276
Pérez, C., Haustein, K., Janjic, Z., Jorba, O., Huneeus, N., Baldasano, J. M., Black, T., Basart, S., Nickovic, S., Miller, R. L., Perlwitz, J. P., Schulz, M., and Thomson, M.: Atmospheric dust modeling from meso to global scales with the online NMMB/BSC-Dust model – Part 1: Model description, annual simulations and evaluation, Atmos. Chem. Phys. Discuss., 11, 17551–17620, doi:10.5194/acpd-11-17551-2011, 2011. 30275, 30277, 30278, 30296, 30299
Prospero, J. M., Ginoux, P., Torres, O., Nicholson, S. E., and Gill, T. E.: Environmental char-

ACPD
11, 30273–30331, 2011

acterization of global sources of atmospheric soil dust identified with the NIMBUS 7 total ozone mapping spectrometer (TOMS) absorbing aerosol product, Rev. Geophys., 40(1), 1002, doi:10.1029/2000RG000095, 2002. 30282

Remer, L. A., Kaufman, Y. J., Tanré, D., Mattoo, S., Chu, D. A., Martins, J. V., Li, R. R., Ichoku, C., Levy, R. C., Kleidman, R. G., Eck, T. F., Vermote, E., and Holben, B. N.: The MODIS aerosol algorithm, products and validation, J. Atmos. Sci., 62, 947–973, 2005. 30284

Rodell, M., Houser, P. R., Jambor, U., Gottschalck, J., Mitchell, K., Meng, C. J., Arsenault, K., Cosgrove, B., Radakovich, J., Bosilovich, M., Entin, J. K., Walker, J. P., Lohmann, D., and Toll, D.: The global land data assimilation system, B. Am. Meteorol. Soc., 85(3), 381–394, 2004. 30280

Schepanski, K., Tegen, I., Laurent, B., Heinold, B., and Macke, A.: A new Saharan dust source activation frequency map derived from MSG-SEVIRI IR-channels, Geophys. Res. Lett., 34(L18803), 168, doi:10.1029/2007GL030168, 2007. 30283

Schepanski, K., Tegen, I., Todd, M. C., Heinold, B., Bönisch, G., Laurent, B., and Macke, A.: Meteorological processes forcing Saharan dust emission inferred from MSG-SEVIRI observations of subdaily dust source activation and numerical models, J. Geophys. Res., 114(D10201), 325, doi:10.1029/2008JD010325, 2009. 30283

Schladitz, A., Müller, T., Kaaden, N., Massling, A., Kandler, K., Ebert, M., Weinbruch, S., Deutscher, C., and Wiedensohler, A.: In situ measurements of optical properties at Tinfou (Morocco) during the Saharan Mineral Dust Experiment SAMUM 2006, Tellus B, 61, 64–78, 2009. 30282, 30293

Schmetz, J., Pili, P., Tjemkes, S., Just, D., Kerkmann, J., Rota, S., and Ratier, A.: An introduction to Meteosat Second Generation (MSG), B. Am. Meteorol. Soc., 83, 977–992, 2002. 30283

Schütz, L., Jaenicke, R., and Pietrek, H.: Saharan dust transport over the North Atlantic Ocean, Geol. Soc. Am., Special Papers, 186, 87–100, 1981. 30293

Seifert, P., Ansmann, A., Mattis, I., Wandinger, U., Tesche, M., Engelmann, R., Müller, D., Pérez, C., and Haustein, K.: Saharan dust and heterogeneous ice formation: eleven years of cloud observations at a Central European EARLINET site, J. Geophys. Res., 115(D20201), 222, doi:10.1029/2009JD013222, 2010. 30276

Slinn, W.: Predictions for particle deposition to vegetative surfaces, Atmos. Environ., 16, 1785–1794, 1982. 30280

Sokolik, I. N. and Toon, O. B.: Direct radiative forcing by anthropogenic airborne mineral aerosols, Nature, 381, 681–683, 1996. 30276

ACPD
11, 30273–30331, 2011

Tanaka, T. Y. and Chiba, M.: Global Simulation of Dust Aerosol with a Chemical Transport Model, MASINGA R, J. Meteorol. Soc. Jpn. A, 83, 255–278, 2005. 30276

Tegen, I.: Modeling the mineral dust aerosol cycle in the climate system, Quaternary Sci. Rev., 22, 1821–1834, 2003. 30276

Tegen, I., Harrison, S. P., Kohfeld, K., Prentice, I. C., Coe, M., and Heimann, M.: Impact of vegetation and preferential source areas on global dust aerosol: results from a model study, J. Geophys. Res., 107(D21), 963, doi:10.1029/2001JD000963, 2002. 30279

Tegen, I., Heinold, B., Todd, M., Helmert, J., Washington, R., and Dubovik, O.: Modelling soil dust aerosol in the Bodélé depression during the BoDEx campaign, Atmos. Chem. Phys., 6, 4345–4359, doi:10.5194/acp-6-4345-2006, 2006. 30277, 30294, 30295

Tesche, M., Ansmann, A., Müller, D., Althausen, D., Mattis, I., Heese, B., Freudenthaler, V., Wiegner, M., Esselborn, M., Pisani, G., and Knippertz, P.: Vertical profiling of Saharan dust with Raman lidars and airborne HSRL in Southern Morocco during SAMU M, Tellus B, 61, 144–164, 2009. 30281, 30289, 30291

Todd, M. C., Washington, R., Martins, J. V., Dubovik, O., Lizcano, G., M'Bainayel, S., and Engelstaedter, S.: Mineral dust emission from the Bodélé Depression, Northern Chad, during BoDEx 2005, J. Geophys. Res., 112(D06 207), 170, doi:10.1029/2006JD007, 2007. 30277, 30282, 30294

Todd, M. C., Bou Karam, D., Cavazos, C., Bouet, C., Heinold, B., Baldasano, J. M., Cautenet, G., Koren, I., Pérez, C., Solmon, F., Tegen, I., Tulet, P., Washington, R., and Zakey, A.: Quantifying uncertainty in estimates of mineral dust flux: an intercomparison of model performance over the Bodélé Depression, Northern Chad, J. Geophys. Res., 113(D24107), 476, doi:10.1029/2008JD010, 2008a. 30277, 30283, 30294

Todd, M. C., Washington, R., Raghavan, S., Lizcano, G., and Knippertz, P.: Regional model simulations of the Bodélé Low-Level Jet of Northern Chad during the Bodélé Dust Experiment (BoDEx 2005), J. Climate, 21, 5, 995–1013, 2008b. 30283, 30294, 30297, 30298

Torres, O., Tanskanen, T., Veihelmann, B., Ahn, C., Braak, R., Bhartia, P. K., Veefkind, P., and Levelt, P.: Aerosols and surface UV products from Ozone Monitoring Instrument observations: an overview, J. Geophys. Res., 112(D24S47), 809, doi:10.1029/2007JD008, 2007. 30283

Washington, R. and Todd, M. C.: Atmospheric controls on mineral dust emission from the Bodele Depression, Chad: the role of the low level jet, Geophys. Res. Lett., 32(L17701), 597, doi:10.1029/2005GL023597, 2005. 30297, 30298

ACPD
11, 30273–30331, 2011

Washington, R., Todd, M. C., Engelstaedter, S., M'bainayel, S., and Mitchell, F.: Dust and the low-level circulation over the Bodélé Depression, Chad: observations from BoDEx 2005, J. Geophys. Res., 111(D03201), 502, doi:10.1029/2005JD006, 2006a. 30277, 30283, 30293, 30294, 30297, 30298

Washington, R., Todd, M. C., Lizcano, G., Tegen, I., Flamant, C., Koren, I., Ginoux, P., Engelstaedter, S., Bristow, C. S., Zender, C. S., Goudie, A. S., Warren, A., and Prospero, J. M.: Links between topography, wind, deflation, lakes and dust: the case of the Bodele Depression, Chad, Geophys. Res. Lett., 33(L09401), 827, doi:10.1029/2006GL025827, 2006b. 30293

Washington, R. W., Todd, M. C., Middleton, N., and Goudie, A. S.: Dust-storm source areas determined by the total ozone monitoring spectrometer and surface observations, Ann. Assoc. Am. Geogr., 93, 297–313, 2003. 30278, 30282

Weinzierl, B., Petzold, A., Esselborn, M., Wirth, M., Rasp, K., Kandler, K., Schütz, L., Koepke, P., and Fiebig, M.: Airborne measurements of dust layer properties, particle size distribution and mixing state of Saharan dust during SAMUM 2006, Tellus, 61B, 96–117, 2009. 30282, 30291

White, B. R.: Soil transport by winds on Mars, J. Geophys. Res., 84(B9), 4643–4651, 1979. 30279

Yin, D., Nickovic, S., Barbaris, B., Chandy, B., and Sprigg, W.: Modeling wind-blown desert dust in the Southwestern United States for public health warning: a case study, Atmos. Environ., 39, 6243–625, 2005. 30276

Zender, C. S., Bian, H., and Newman, D.: Mineral Dust Entrainment and Deposition (DEAD) model: description and 1990s dust climatology, J. Geophys. Res., 108, 4416, doi:10.1029/2002JD002775, 2003. 30295

Zender, C. S., Newman, D., and Torres, O.: Spatial heterogeneity in aeolian erodibility: uniform, topographic, geomorphic, and hydrologic hypotheses, J. Geophys. Res., 108(D17), 4543, doi:10.1029/2002JD003039, 2003b. 30280

Zender, C. S., Miller, R. L., and Tegen, I.: Quantifying mineral dust mass budgets: terminology, constraints, and current estimates, Electron. Suppl. (EOS), 85(48), 509–512, 2004. 30276

Zhang, L., Gong, S., Padro, J., and Barrie, L.: A size-segregated particle dry deposition scheme for an atmospheric aerosol module, Atmos. Environ., 35, 549–560, 2001. 30280

Zhao, C., Liu, X., Leung, L. R., Johnson, B., McFarlane, S. A., Gustafson Jr., W. I., Fast, J. D., and Easter, R.: The spatial distribution of mineral dust and its shortwave radiative forcing over

ACPD
11, 30273–30331, 2011

North Africa: modeling sensitivities to dust emissions and aerosol size treatments, Atmos. Chem. Phys., 10, 8821–8838, doi:10.5194/acp-10-8821-2010, 2010. 30284

ACPD
11, 30273–30331, 2011

Table 1. Location of all AERONET and EARLINET stations including the BoDEx station Chicha in the Bodélé depression.

Acron.	Location	Altitude	Latitude	Longitude
PAL	Palencia	743 m	41.99° N	4.51° W
SAA	Saada	1890 m	31.63° N	8.16° W
OUZ	Ouarzazate	1150 m	30.94° N	6.91° W
ZAG	Zagora	730 m	30.33° N	5.84° W
BLI	Blida	230 m	36.51° N	2.88° E
LAM	Lampedusa	50 m	35.52° N	12.63° E
TMR	Tamanrasset	1400 m	22.79° N	5.53° E
BAN	Banizoumbou	250 m	13.54° N	2.66° E
BOD	Chicha	179 m	17.0° N	18.0° E
NAP	Naples	118 m	40.84° N	14.18° E
THE	Thessaloniki	60 m	40.63° N	22.95° E
ATH	Athens	200 m	37.96° N	23.78° E

ACPD
11, 30273–30331, 2011

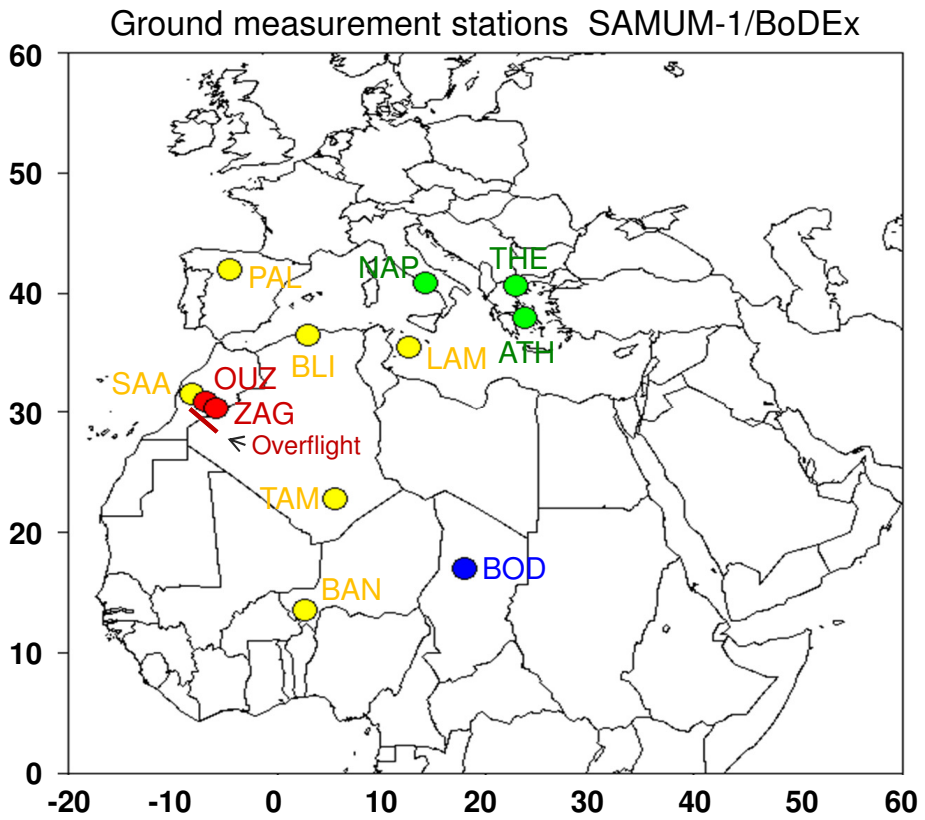

Fig. 1. Overview of all ground measurement stations within the model simulation domain used in this paper. Red dots are the SAMUM-1 field sites Ouarzazate (OUZ) and Zagora (ZAG), yellow dots are AERONET stations, the blue dot is the BoDEx field site Chicha, and the green spots are EARLINET lidar stations. The Falcon overflight path just south of Ouarzazate and Zagora is shown in red.

ACPD
11, 30273–30331, 2011

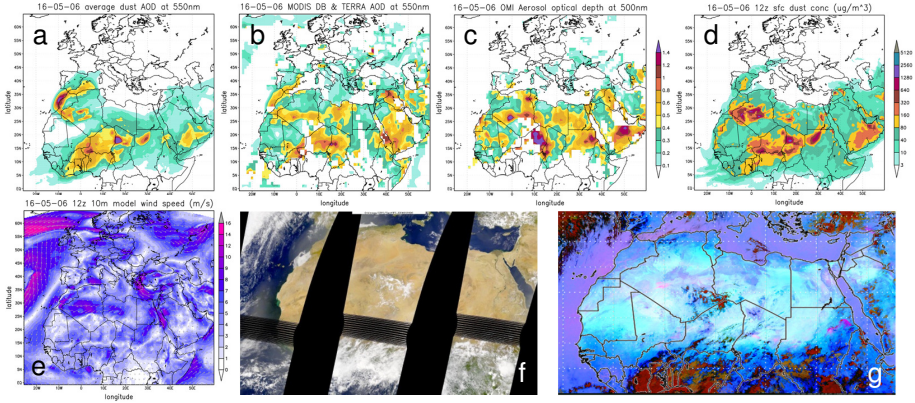

Fig. 2. Four hour average AOD from NMMB/BSC-Dust **(a)**, MODIS Deep Blue and Terra **(b)**, OMI AOD **(c)**, model derived surface dust concentration at 12*z* **(d)**, model derived 10 m wind speed at 12*z* **(e)**, the SeaWIFS VIS image at 12*z* **(f)**, and the MSG dust image at 12*z* **(g)** on 16 May 2006 are displayed for the North African domain.

ACPD
11, 30273–30331, 2011

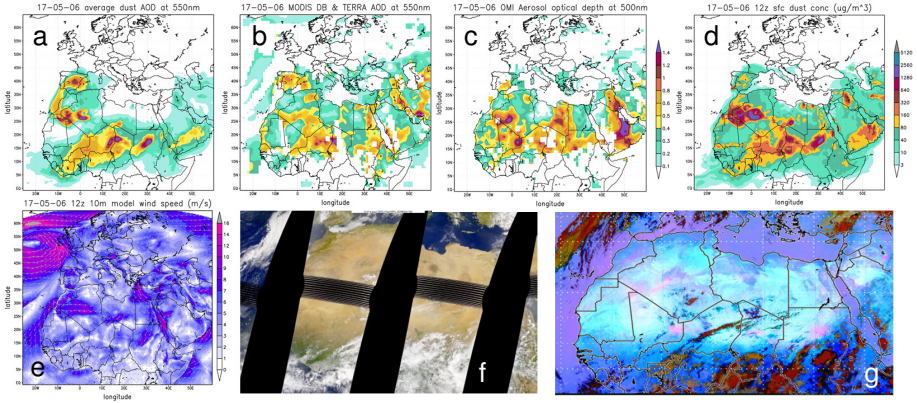

Fig. 3. Four hour average AOD from NMMB/BSC-Dust **(a)**, MODIS Deep Blue and Terra **(b)**, OMI AOD **(c)**, model derived surface dust concentration at 12*z* **(d)**, model derived 10 m wind speed at 12*z* **(e)**, the SeaWIFS VIS image at 12*z* **(f)**, and the MSG dust image at 12*z* **(g)** on 17 May 2006 are displayed for the North African domain.

ACPD
11, 30273–30331, 2011

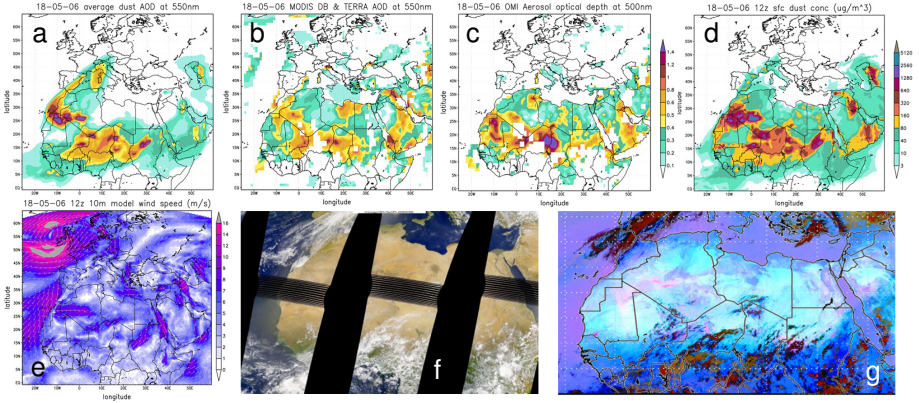

Fig. 4. Four hour average AOD from NMMB/BSC-Dust **(a)**, MODIS Deep Blue and Terra **(b)**, OMI AOD **(c)**, model derived surface dust concentration at 12*z* **(d)**, model derived 10 m wind speed at 12*z* **(e)**, the SeaWIFS VIS image at 12*z* **(f)**, and the MSG dust image at 12*z* **(g)** on 18 May 2006 are displayed for the North African domain.

ACPD
11, 30273–30331, 2011

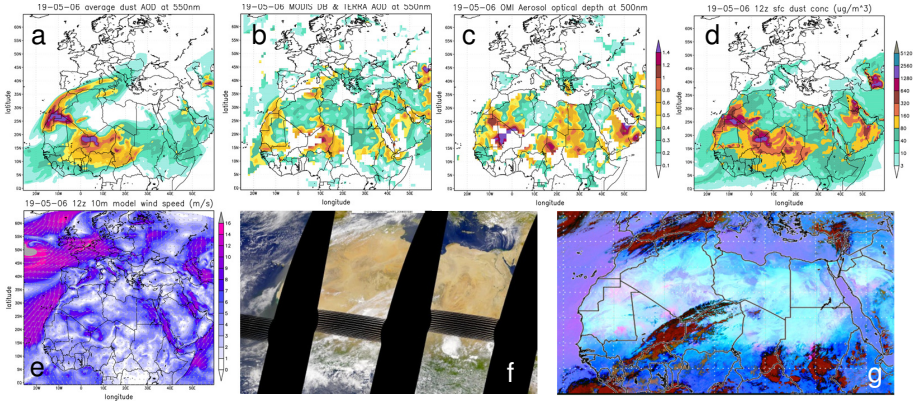

Fig. 5. Four hour average AOD from NMMB/BSC-Dust **(a)**, MODIS Deep Blue and Terra **(b)**, OMI AOD **(c)**, model derived surface dust concentration at 12*z* **(d)**, model derived 10 m wind speed at 12*z* **(e)**, the SeaWIFS VIS image at 12*z* **(f)**, and the MSG dust image at 12*z* **(g)** on 19 May 2006 are displayed for the North African domain.

ACPD
11, 30273–30331, 2011

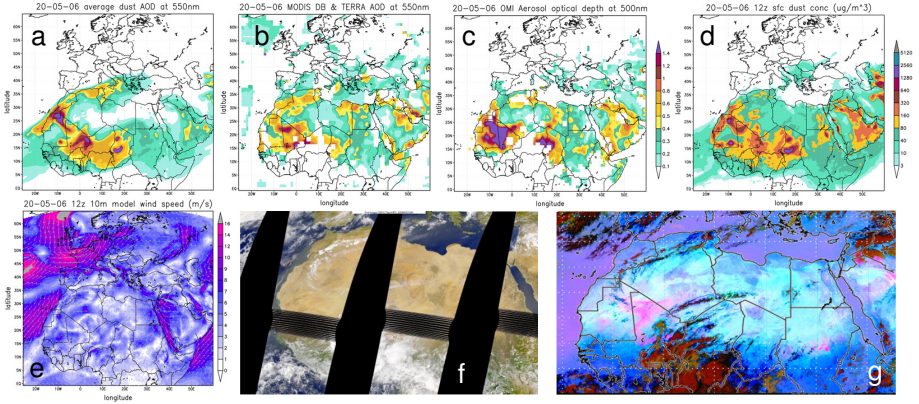

Fig. 6. Four hour average AOD from NMMB/BSC-Dust **(a)**, MODIS Deep Blue and Terra **(b)**, OMI AOD **(c)**, model derived surface dust concentration at 12*z* **(d)**, model derived 10 m wind speed at 12*z* **(e)**, the SeaWIFS VIS image at 12*z* **(f)**, and the MSG dust image at 12*z* **(g)** on 20 May 2006 are displayed for the North African domain.

ACPD
11, 30273–30331, 2011

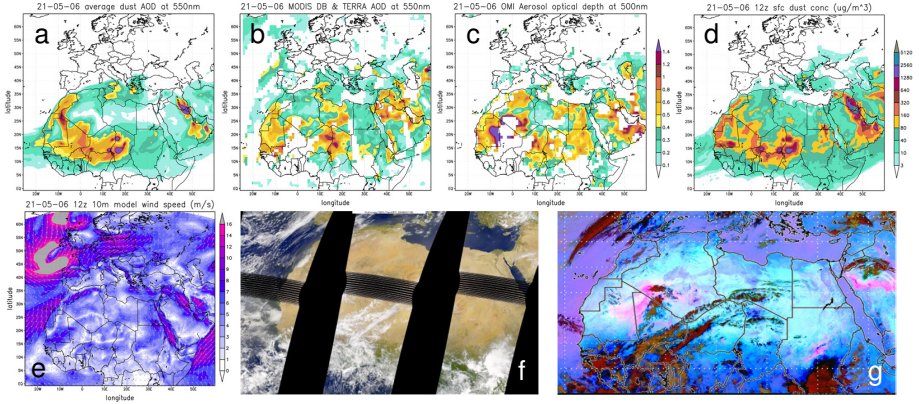

Fig. 7. Four hour average AOD from NMMB/BSC-Dust **(a)**, MODIS Deep Blue and Terra **(b)**, OMI AOD **(c)**, model derived surface dust concentration at 12*z* **(d)**, model derived 10 m wind speed at 12*z* **(e)**, the SeaWIFS VIS image at 12*z* **(f)**, and the MSG dust image at 12*z* **(g)** on 21 May 2006 are displayed for the North African domain.

ACPD
11, 30273–30331, 2011

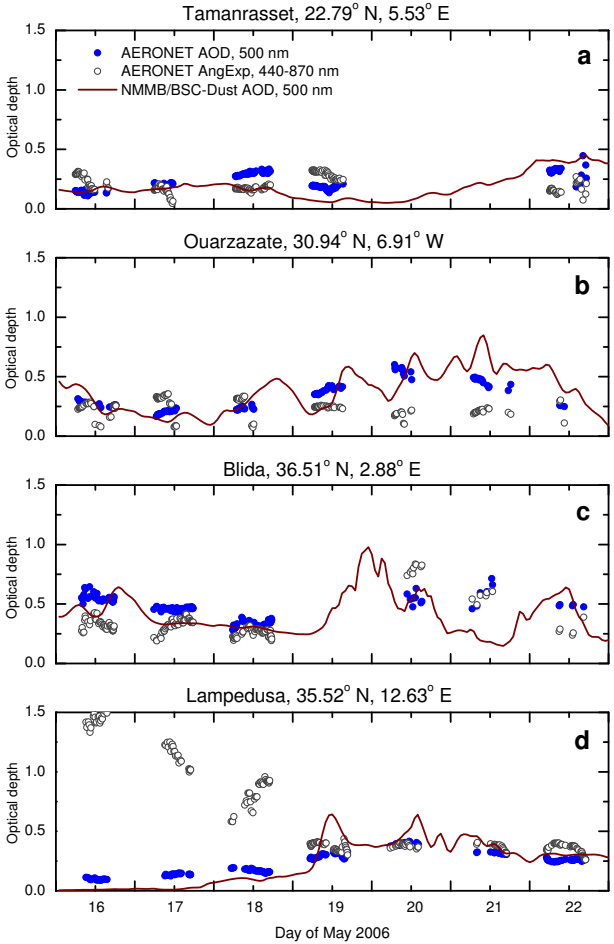

Fig. 8. Model derived AOD (brownish line) versus AERONET AOD (blue dots) and Ångström exponent for the period of 16–22 May at Tamanrasset **(a)**, Ouarzazate **(b)**, Blida **(c)**, and Lampedusa **(d)**.

ACPD
11, 30273–30331, 2011

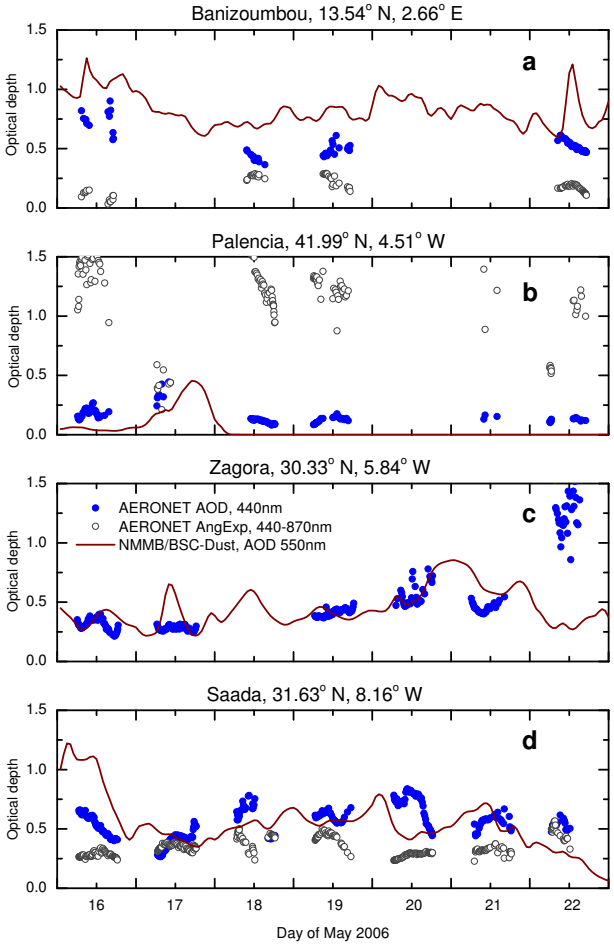

Fig. 9. Model derived AOD (brownish line) versus AERONET AOD (blue dots) and Ångström exponent for the period of 16–22 May at Banizoumbou **(a)**, Palencia **(b)**, Zagora **(c)**, and Saada **(d)**.

ACPD
11, 30273–30331, 2011

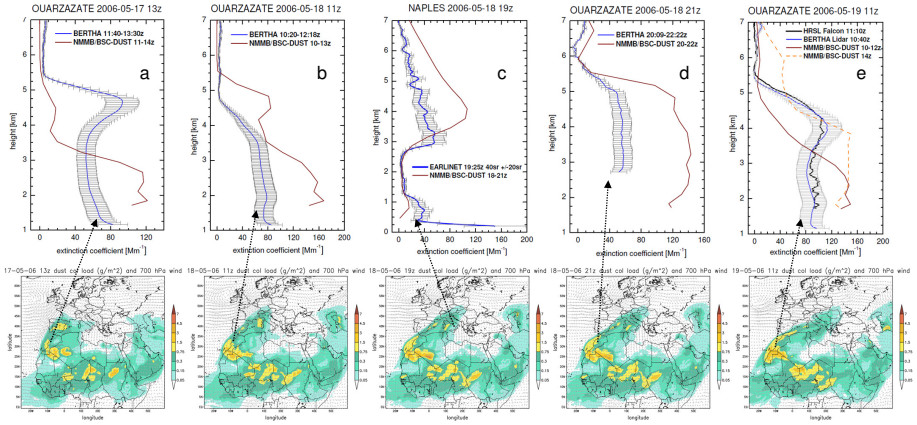

Fig. 10. Measured (blue line) and model derived (brownish line) vertical profiles (height above sea level) of the extinction coefficient at European and North African stations: Measurements at Ouarzazate **(a,b,d,e)** are taken during the SAMUM-1 campaign with BERTHA lidar, while Naples **(c)** representing an EARLINET station. Profiles are shown for the period between 17–19 May 2006. Note that overflight HSRL Lidar is shown at 19 May over Ouarzazate **(j)**. Below the vertical profiles, the simulated dust column load and the 700 hPa wind for the European domain for each date is displayed. The model is driven with NCEP-FNL 1° × 1° analysis meteorology data.

ACPD
11, 30273–30331, 2011

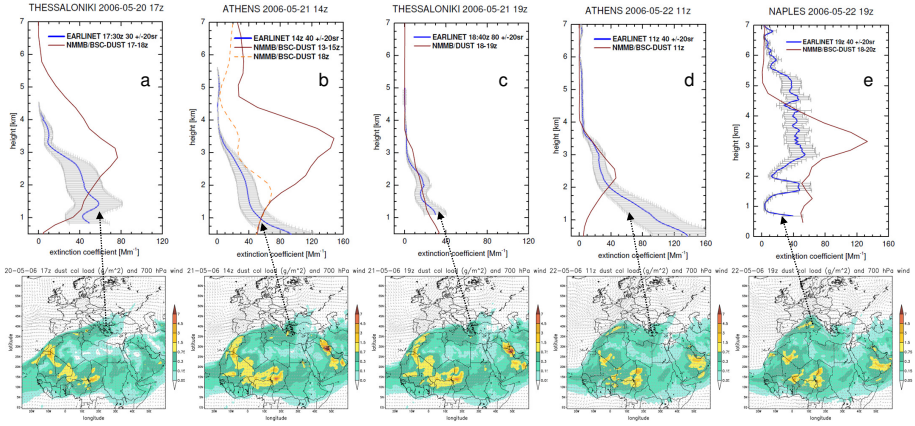

Fig. 11. Measured (blue line) and model derived (brownish line) vertical profiles (height above sea level) of the extinction coefficient at European stations: Measurements are taken from EARLINET stations in Athens **(g,j)**, Naples **(k)**, and Thessaloniki **(f,h)**. Profiles are shown for the period between 20–22 May 2006. Below the vertical profiles, the simulated dust column load and the 700 hPa wind for the European domain for each date is displayed. The model is driven with NCEP-FNL 1° × 1° analysis meteorology data.

ACPD
11, 30273–30331, 2011

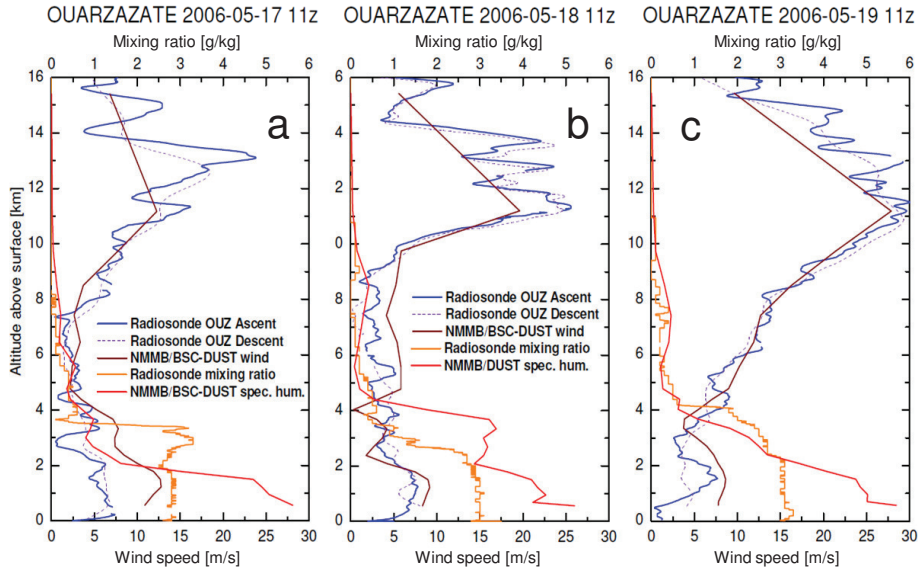

Fig. 12. Vertical profile of wind speed (blue, brown), specific humidity (red) or mixing ratio (orange), respectively, over Ouarzazate between 17–19 May 2006 is shown **(a–c)**. Comparison of simulated winds versus that derived from morning radiosonde launch.

ACPD
11, 30273–30331, 2011

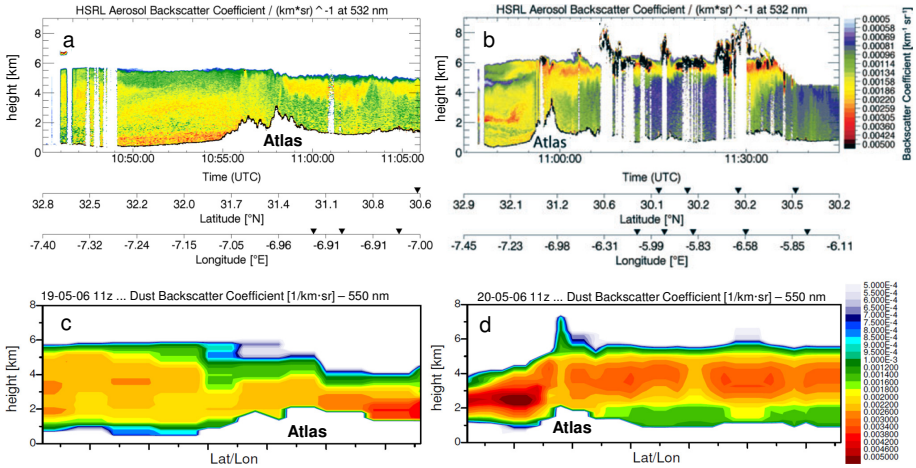

Fig. 13. Vertical cross-section of dust backscatter coefficient during the Falcon overflight from Casablanca to Ouarzazate on 19 and 20 May 2006. Lidar data from Falcon flight measurements **(a,b)** versus model-derived backscatter coefficient at 550 nm **(c,d)** are shown. Arrows on the longitude/latitude axis indicate changes in the flight direction of the aircraft.

ACPD
11, 30273–30331, 2011

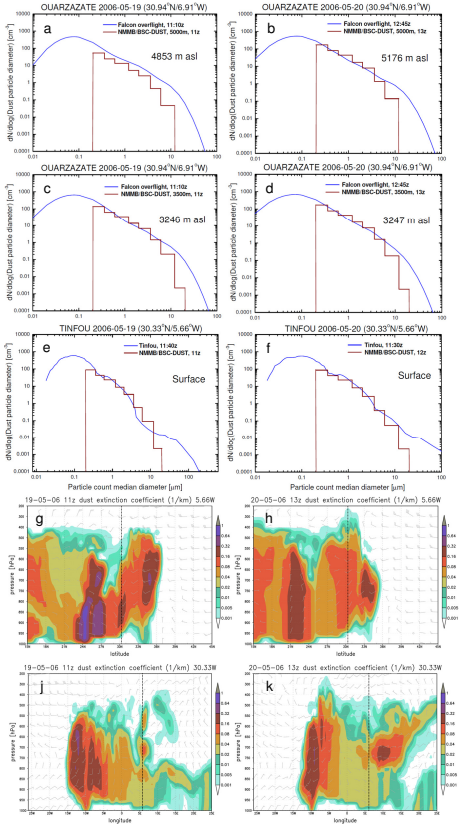

Fig. 14. Measured (blue line) and model derived particle size distribution (brownish line) at 19 and 20 May 2006 over Ouarzazate at 5 km **(a,b)** and 3 km **(c,d)** altitude, and at the surface in Tinfou **(e,f)**. Notice the truncated ordinate, causing the largest model size class to be out of range **(a,b)**. Complementary, the latitudinal **(g,h)** and the longitudinal **(j,k)** model extinction cross-section and wind bars are shown. The location of the Tinfou/Ouarzazate region is marked with the dotted line.

ACPD
11, 30273–30331, 2011

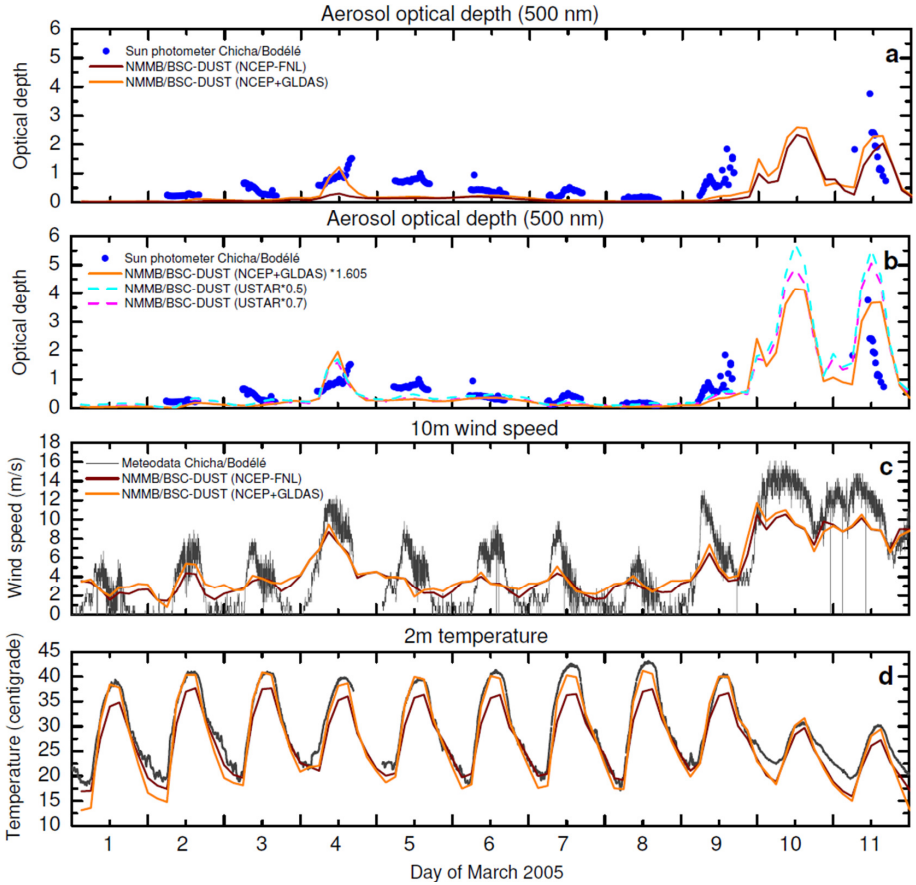

Fig. 15. Model derived AOD, 10 m wind speed and 2 m temperature (brown and orange solid lines) over the Bodélé versus AOD from Sun photometer (blue dots) **(a, b)** and wind speed **(c)** and temperature from meteorological observations (blue solid line) **(d)** at Chicha for the period 1–11 March 2005. The dashed cyan and pink lines **(b)** refer to the alternative model setup as indicated in the legend.

ACPD
11, 30273–30331, 2011

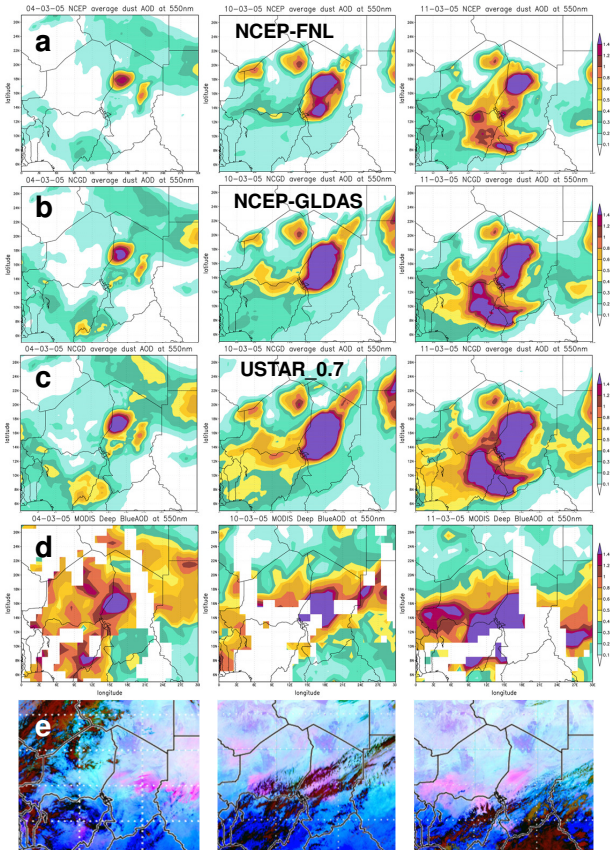

Fig. 16. Four hour average of model AOD for the 3 experiments: NCEP-FNL **(a)**, NCEP-GLDAS **(b)**, NCEP-GLDAS with reduced threshold friction velocity **(c)**. MODIS DB AOD **(d)** and MSG dust image at 12*z* **(e)** on 4, 10, 11 March 2005 are displayed for the limited regional domain (5° N to 27° N and 0° W to 30° E).

ACPD
11, 30273–30331, 2011

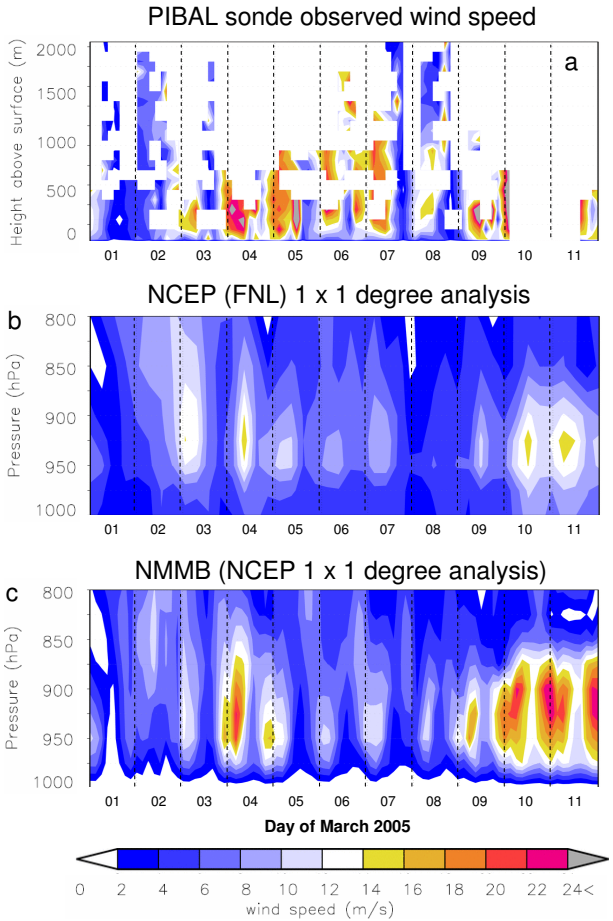

Fig. 17. Time-height profile of wind speed ($m\,s^{-1}$) at Chicha as derived from PIBAL balloon data **(a)**, NCEP analysis $1^{\circ} \times 1^{\circ}$ data **(b)** and NMMB/BSC-Dust initialized with NCEP analysis and GLDAS soil conditions **(c)** for the period from 1–11 March 2005. Note that height units are either given in m or hPa.

ACPD
11, 30273–30331, 2011